



HAL
open science

A Bayesian approach for the estimation of the thermal diffusivity of aerodynamically levitated solid metals at high temperatures

Bernard Lamien, Dylan Le Maux, Mickael Courtois, Thomas Pierre, Muriel Carin, Philippe Le Masson, Helcio Rangel Barreto Orlande, Pascal Paillard

► To cite this version:

Bernard Lamien, Dylan Le Maux, Mickael Courtois, Thomas Pierre, Muriel Carin, et al.. A Bayesian approach for the estimation of the thermal diffusivity of aerodynamically levitated solid metals at high temperatures. *International Journal of Heat and Mass Transfer*, 2019, 141, pp.265-281. 10.1016/j.ijheatmasstransfer.2019.06.054 . hal-02290940

HAL Id: hal-02290940

<https://hal.science/hal-02290940>

Submitted on 25 Oct 2021

HAL is a multi-disciplinary open access archive for the deposit and dissemination of scientific research documents, whether they are published or not. The documents may come from teaching and research institutions in France or abroad, or from public or private research centers.

L'archive ouverte pluridisciplinaire **HAL**, est destinée au dépôt et à la diffusion de documents scientifiques de niveau recherche, publiés ou non, émanant des établissements d'enseignement et de recherche français ou étrangers, des laboratoires publics ou privés.



Distributed under a Creative Commons Attribution - NonCommercial 4.0 International License

A BAYESIAN APPROACH FOR THE ESTIMATION OF THE THERMAL DIFFUSIVITY OF AERODYNAMICALLY LEVITATED SOLID METALS AT HIGH TEMPERATURES

**Bernard Lamien^{1,2,3*}, Dylan Le Maux¹, Mickael Courtois¹, Thomas Pierre¹,
Muriel Carin¹, Philippe Le Masson¹, Helcio Rangel Barreto Orlando², Pascal Paillard³**

¹Univ. Bretagne Sud, UMR CNRS 6027, IRDL, F-56100 Lorient, France

²Department of Mechanical Engineering, DEM/PEM – Politécnica/COPPE
Federal University of Rio de Janeiro – UFRJ

Caixa Postal: 68503, Cidade Universitária, Rio de Janeiro, RJ, 21941-972, Brazil

Phone: +55-21-3938-8405; Fax: +55-21-3938-8383

³IMN-CNRS, Rue de la Houssinière, Nantes, France

bernard.lamien@univ-ubs.fr, dylan.le-maux@univ-ubs.fr, mickael.courtois@univ-ubs.fr,
thomas.pierre@univ-ubs.fr, muriel.carin@univ-ubs.fr, philippe.le-masson@univ-ubs.fr,
helcio@mecanica.coppe.ufrj.br, pascal.paillard@univ-nantes.fr

Abstract

The flash method has been the standard technique for the measurement of thermal diffusivity since it was first developed by Parker and co-workers. Several modifications of the original method have been proposed in the literature, to deal with different physical situations and materials. In this work, we extend the front-face flash method for the simultaneous estimation of the thermal diffusivity and thermal conductivity of aerodynamically levitated spherical solid metal samples at high temperatures, with laser excitation and contactless temperature measurements taken with a pyrometer. The mathematical model associated to the physical problem is formulated as an axisymmetric heat conduction problem, with heat losses by radiation and convection. Since the measurements of a pyrometer are in fact radiative fluxes, the transfer function of the pyrometer is integrated in the mathematical model. A sensitivity analysis is performed and reveals that the thermal diffusivity and the thermal conductivity of the sample can be simultaneously estimated, provided that the other model parameters are known. The solution of the inverse problem is obtained with algorithms within the Bayesian framework of statistics, by using a heat conduction reduced model with linear boundary conditions, for which an analytical solution is developed for fast computations. The Bayesian Approximation Error Model is used to compensate for errors between a complete heat conduction model with nonlinear boundary conditions and a reduced heat conduction model with linear boundary conditions. Moreover, errors related to the inaccuracy and the uncertainties of all model parameters are accounted for in the inverse analysis. Simulated transient flux measurements are assumed available from a multi-spectral pyrometer and are used for the inverse problem solution.

Keywords: *thermal diffusivity, thermal conductivity, flash method, aerodynamic levitation, Bayesian estimator*

* Corresponding author

NOMENCLATURE

A	Metropolis-Hastings ratio
Bi	Biot number
f	laser source spatial and temporal distribution
F_{d1-2}	form factor between a differential surface element and a finite surface
H_{Mi}	amplitude correction of the pyrometer transfer function
J	reduced dimensionless sensitivity coefficients
\mathbf{J}	sensitivity matrix computed with the complete model
k	thermal conductivity
M_{λ}^0	black body emittance
P	parameter
\mathbf{P}	vector of sought parameters
q_0	maximum laser radiation flux
r	radial coordinate within the sphere
r_0	Gaussian radius of the laser beam
R	sphere radius
S_{ref}	reference surface observed by the pyrometer
S_V	surface observed by the pyrometer
T	temperature
\mathbf{X}	sensitivity matrix computed with the reduced model
\mathbf{Y}	vector of measurements
\mathbf{Z}	vector of auxiliary parameters

Greek Symbols

α	thermal diffusivity
ε	emissivity
κ	absorptivity
θ	polar angle in the sphere
θ_{spot}	location of the extreme point of the surface observed by the pyrometer
λ	wavelength
μ	transformed θ coordinate, defined as $\cos \theta$
μ_{spot}	cosine of the location of the extreme point of the surface observed by the pyrometer
μ_0	cosine of the incidence angle of the beam
τ	dimensionless time
φ	spherical coordinates
σ	Stefan-Boltzmann constant
Φ	radiative flux
Ψ	vector of the complete set of parameters
$\pi(a b)$	conditional probability density of a when b is given

Subscripts and Superscripts

$conv$	convective
eff	combined convection and radiation
F	quasi-steady state problem
H	problem with homogeneous boundary conditions
h	pulse duration
j	parameter number

<i>rad</i>	radiation
<i>red</i>	reduced
*	dimensionless
0	initial or peak value
λ	spectral
∞	ambient
<i>t</i>	state of the Markov chain
<i>i</i>	index of the measurement time
<i>s</i>	index of a spectral channel of the pyrometer
<i>ref</i>	reference value

1. INTRODUCTION

The measurement of thermophysical properties of metallic materials at high temperatures is very challenging, due to possible chemical reactions between the sample and container, but also due to convection inside the sample in the case of molten metals [1–6]. As a consequence, literature data on the thermophysical properties of metals at high temperatures is far from complete. Accurate thermophysical properties of metals at high temperatures are of great importance for numerical simulations, used for analysis and design of engineering processes like welding and additive manufacturing. Levitation techniques, together with contactless excitation and measurements, have been proposed in order to avoid sample contamination during thermal characterization of metals at high temperatures [1–3,5,7–12]. By using levitation techniques, physical properties, like density, surface tension and viscosity, as well as some structural properties of liquid metals, were successfully measured under terrestrial and microgravity conditions [3,13–15]. On the other hand, as pointed out in the literature[3,16], the measurement of transport properties, like diffusion coefficient and thermal diffusivity of molten metals in containerless environment, are prone to measurement errors due to unavoidable convective effects.

Thermal diffusivity is commonly measured with the flash method, a technique developed by Parker and co-workers [17], which is an ASTM standard [18]. The basic flash method consists in uniformly heating a thin sample with a short light pulse on its front surface and measuring the temperature rise at the rear surface. The measured temperature rise is then compared with a theoretical temperature profile obtained from the solution of a one-dimensional heat conduction model and the thermal diffusivity can be identified from simple algebraic equations or via parameter estimation [2,19–26]. Extensions of the flash method were proposed in order to deal with different physical situations, including levitated metals, in solid and liquid states, at high temperatures [1,2,27]. In some of these works, advanced thermal models for the flash method, together with inverse parameter estimation techniques, were used for the estimation of the thermal diffusivity. These advanced thermal models require other auxiliary model parameters, which are not of primary interest but must be known for an accurate estimation of the thermal diffusivity. A common feature of these previous works is that the solution of the inverse problem was obtained by considering the auxiliary parameters as deterministically “known”. Therefore, the values estimated for the thermal diffusivity did not reflect actual uncertainties in the judged “known” model parameters. On the other hand, the solution of inverse problems within the Bayesian

framework of statistics can cope with uncertainties of all parameters appearing in the mathematical formulation of the physical problem [28,29]. Although very robust, the computational cost related to the solution of inverse problems within the Bayesian framework can be very high and one might need to use reduced order models. The proposed Bayesian Approximation Error approach, referred to as AEM [28], allows for the use of reduced order models by constructing a statistical model for the modelling errors, which are treated as an additional noise in the measurement model. Furthermore, the approach provides an effective way for the treatment of uncertainties related to auxiliary parameters [28–33].

In this paper, a methodology is proposed for the extension of the front-face flash method to aerodynamically levitated metal samples in the solid state and at high temperatures. The theoretical model is based on a transient two-dimensional heat conduction problem, with axial symmetry and with heat losses by radiation and convection. Simulated transient radiative flux measurements are assumed available from a multispectral pyrometer, for the inverse analysis. Since the pyrometer measures radiative fluxes, the approach developed here integrates its transfer function in the theoretical model. The inverse parameter estimation problem in this work deals with the simultaneous estimation of thermal diffusivity and thermal conductivity of the levitating metal sample. The inverse problem is solved within the Bayesian framework of statistics, which allows that uncertainties related to the auxiliary parameters be considered in the analysis. Similarly, modelling errors resulting from the use of a reduced model, instead of a complete model, are appropriately accounted for, with the Bayesian approximation error approach. The main purpose of this paper is to demonstrate the feasibility of the proposed methodology for estimating simultaneously the thermal diffusivity and the thermal conductivity of a levitating metal sample at high temperatures. This work is under development and is built upon the experimental facility described next.

2. EXPERIMENTAL SETUP

For the thermal characterization of metallic materials, in solid or liquid states at high temperatures, an experimental facility using aerodynamic levitation of samples was developed. Aerodynamic levitation is chosen as the containerless technique for this setup because it is independent of the heating system and of the acoustic excitation, which are used for the flash method and for the measurements of viscosity and surface tension. A gas (argon) is blown from below on a spherical-shaped sample of metal in the solid or liquid state, of a few millimeters in diameter, through a conical nozzle of 60° , in order to counterbalance the effect of gravity and to levitate the sample (see figure 1). The nozzle is made of boron nitride

because of its low wettability, which avoids attachment of the sample in the liquid state. Furthermore, the high melting point of boron nitride avoids a dedicated cooling system for the nozzle. Another choice of material for the nozzle is copper owing to its high thermal conductivity and low emissivity. A Ytterbium fibre laser (1 070 nm) of maximal output power 300 W (CW mode) from IPG Photonics providing a Gaussian intensity distribution is used for heating the metal sample, as well as for providing the pulse for the Flash method.

Figure 1 presents the experimental setup. A cubical enclosure of dimension 15cmx15cmx15cm keeps the sample in a non-oxidizing environment. Four windows of the enclosure, made of silicate boron or sapphire, enable the laser heating and the measurements. Through the top window, the sample can be heated continuously by the laser to temperatures ranging from 20 °C to 3 500 °C, then the heating is ceased and the sample is let to cool-down to the desired high initial temperature, which is below the melting point. With the heating ceased, the levitated sample of metal owing to its high thermal conductivity and its small size (3 mm) rapidly satisfy the lumped body assumption ($Biot < 0.1$). Thus, the initial temperature of the sample can be considered as uniform. When the sample reaches the desired initial temperature, a short laser pulse is used for the thermal diffusivity measurement, such as in the flash method. A fast optical camera (Photron SA5) is mounted with macro lenses at one of the lateral sides of the cubical enclosure. This fast optical camera operates at 1 kHz to measure morphological changes of the sample, or contamination of the sample surface. The analysis of the acquired optical images allow for the measurement of density as a function of temperature, as well as the viscosity and the surface tension through an oscillatory acoustic excitation of the sample in liquid state [34–36]. An infrared camera (FLIR X6580sc) is used for temperature measurements, through one of the lateral windows. Finally, part of the sample radiative emission goes through the sapphire window on the top of the cubical enclosure and is collected by a multispectral pyrometer, after passing through a collimator. With the help of dichroic mirrors, this pyrometer separates the collected radiative flux in the direction of six monochromatic filters with photodetectors that measure quasi-monochromatic fluxes at mean wavelengths of 480 nm, 530 nm, 680 nm, 850 nm, 940 nm and 1 550 nm.

The pyrometer transfer function, which relates the theoretical flux at each photodetector to the flux emitted from the surface of the sample that reaches the pyrometer and is collected by the collimator, is given by assuming an opaque and diffuse surface and a nonparticipating surrounding medium as [37,38]:

$$\Phi_s(t) = \varepsilon_{\lambda,pyro} F_{d1-2} \int_{\bar{\lambda}_i - 3\sigma_{\lambda_i}}^{\bar{\lambda}_i + 3\sigma_{\lambda_i}} \int_{S_V} M_{\lambda}^0(T) H_{Mi} e^{-\frac{1}{2} \left(\frac{\lambda - \bar{\lambda}_i}{\sigma_{\lambda_i}} \right)^2} d^2 S_k d\lambda \quad (1)$$

where $\varepsilon_{\lambda,pyro}$ is the normal spectral emissivity of the sample at the mean wavelength of the photodetector, $M_{\lambda}^0(T)$ is the emittance of the sample at temperature T , F_{d1-2} represents the view factor between a differential surface element on the sample surface seen by the pyrometer and the disk-shaped collimator, and is readily obtained from [39,40], while the exponential function represents the Gaussian-shaped monochromatic filters centred on $\bar{\lambda}_i$ and with standard deviation σ_{λ_i} . H_{Mi} is an amplitude correction of the transfer function for each wavelength of the pyrometer, and accounts for radiative flux losses in the optical system of the pyrometer and other non-quantifiable factors. A calibration of the pyrometer was performed, aiming at obtaining an estimate of the parameters H_{Mi} , by comparing the theoretical flux given by equation (1) to the measured flux for selected experiments. This calibration procedure for the temperature range of 900°C - 2500°C, obtained with pure metals at their melting points, was reported by the authors in [38].

3. PHYSICAL PROBLEM AND MATHEMATICAL FORMULATION

The physical model associated to the experimental setup described above for the extended front-face flash method assumes a levitating solid metal in the form of a sphere, initially at an elevated and uniform temperature T_0 , and then subjected to a short pulse laser irradiation with Gaussian spatial profile and temporal profile $u(t)$ given as,

$$Q(r_b, t) = q_0 u(t) \exp\left(\frac{-2r_b^2}{r_0^2}\right) \quad (2)$$

where q_0 is the maximum laser radiation flux, r_b is the radial distance from the center of the beam, and r_0 is the Gaussian radius of the beam, as illustrated by figure 2(a). The temporal profile of the laser source is either a square pulse (figure 2(b)) or an exponentially decaying pulse (figure 2(c)). The incident laser beam is assumed co-axial with the levitating metal, so that the problem can be formulated as two-dimensional with axial symmetry. The levitated solid metal exchange heat with the surroundings by radiation and convection [2]. The measurements used in this work are the radiative fluxes collected by the multispectral pyrometer. Hence, the approach proposed here integrates the pyrometer transfer functions (1) in the theoretical model.

Hereafter two models, referred to as the complete model and the reduced model, are used to describe the heat transfer process of the extended front-face flash method, for the characterization of metallic materials in solid state at high temperatures, as described below. The thermophysical properties of these two models were supposed constant, since the temperature increase provided by the flash laser is small.

3.1 The complete model

The mathematical formulation of the heat conduction problem in dimensionless form in spherical coordinates (r, θ, φ) , with transformed polar angle $\mu = \cos \theta$ and associated initial and boundary conditions, is given by:

$$\frac{1}{\alpha^*} \frac{\partial T^*(r^*, \mu, \tau)}{\partial \tau} = \frac{1}{r^{*2}} \frac{\partial}{\partial r^*} \left(r^{*2} \frac{\partial T^*(r^*, \mu, \tau)}{\partial r^*} \right) + \frac{1}{r^{*2}} \frac{\partial}{\partial \mu} \left((1-\mu^2) \frac{\partial T^*(r^*, \mu, \tau)}{\partial \mu} \right) \quad \tau > 0, 0 \leq r^* < 1, -1 \leq \mu \leq 1 \quad (3.a)$$

$$k^* \frac{\partial T^*(r^*, \mu, \tau)}{\partial r^*} + Bi_{rad} (T^{*4}(r^*, \mu, \tau) - T_{\infty}^{*4}) + Bi_{conv} (T^*(r^*, \mu, \tau) - T_{\infty}^*) = \kappa_{\lambda, laser} q_0^* f(\mu, \tau, \mu_0, \tau_h) \quad r^* = 1, -1 \leq \mu \leq 1, \tau > 0 \quad (3.b)$$

$$T^*(r^*, \mu, \tau) = 1, 0 \leq r^* \leq 1, -1 \leq \mu \leq 1, \tau = 0 \quad (3.c)$$

where, for the radiative transfer, it was assumed that the surrounding surface is in thermal equilibrium with the gas inside the enclosure. The dimensionless measured radiative flux given by:

$$\Phi_s^*(\tau) = \frac{\varepsilon_{\lambda, pyro} F_{d1-2}}{q_{ref} S_{ref}} \int_{\bar{\lambda}_i - 3\sigma_{\lambda_i}}^{\bar{\lambda}_i + 3\sigma_{\lambda_i}} \int_{S_v} M_{\lambda}^0(T) H_{Ml} e^{-\frac{1}{2} \left(\frac{\lambda - \bar{\lambda}_i}{\sigma_{\lambda_i}} \right)^2} d^2 S_k d\lambda \quad (4)$$

The following dimensionless parameters were introduced for the model formulation:

$$T^* = \frac{T(r, \mu, t)}{T_0}; \quad (5.a)$$

$$T_{\infty}^* = \frac{T_{\infty}}{T_0}; \quad (5.b)$$

$$r^* = \frac{r}{R} ; \quad (5.c)$$

$$\tau = \frac{\alpha_{ref} t}{R^2} \quad (5.d)$$

$$\alpha^* = \frac{\alpha}{\alpha_{ref}} \quad (5.e)$$

$$k^* = \frac{k}{k_{ref}} ; \quad (5.f)$$

$$Bi_{conv} = \frac{h_{conv} R}{k_{ref}} ; \quad (5.g)$$

$$Bi_{rad} = \frac{\epsilon_{losses} \sigma R T_0^3}{k_{ref}} ; \quad (5.h)$$

$$q_0^* = \frac{q_0}{q_{ref}} \quad (5.i)$$

$$\Phi_s^* = \frac{\Phi_s}{q_{ref} S_{ref}} \quad (5.j)$$

with,

$$q_{ref} = \frac{k_{ref} T_0}{R} \quad (5.k)$$

$$S_{ref} = 2\pi R^2 (1 - \mu_{spot}) \quad (5.l)$$

and the subscript *ref* denotes a reference value for the material being characterized. These reference values can be taken from the literature for similar materials. S_{ref} is a reference surface, given by the area of the spherical cap observed by the pyrometer around the symmetry axis. In the formulation of equation (3.b), the boundary heat source term $f(\mu, \tau, \mu_0, \tau_h)$ represents the spatio-temporal profile of the laser excitation (2) written in terms of the transformed polar angle μ and of the dimensionless time τ . The functional form of $f(\mu, \mu_0, \tau, \tau_h)$ was written in terms of the product of functions $g(\mu, \mu_0)$ and $u(\tau, \tau_h)$, representing the spatial and temporal profile, respectively. These functions are given as,

$$g(\mu, \mu_0) = \exp\left(-2 \frac{(1 - \mu^2)}{(1 - \mu_0^2)}\right) \quad (6)$$

for the spatial distribution, while the temporal profile is either a square pulse represented by

$$u(\tau, \tau_h) = \frac{1}{2}(1 + \text{erf}(\phi(\tau - \tau_a))) - \frac{1}{2}(1 + \text{erf}(\phi(\tau - \tau_d))) \quad (7.a)$$

or an exponential decaying pulse

$$u(\tau, \tau_h) = \frac{\tau^2}{4\tau_h^2} \exp\left(2 - \frac{\tau}{\tau_h}\right) \quad (7.b)$$

In the above equations, ϕ is a smoothing parameter ($\phi=2700$), while subscripts “a” and “d” refer to the ascent and descent time of the square pulse.

For the solution of the complete model given by equations (3), the finite element method was used through the COMSOL Multiphysics® 4.3b commercial package.

3.2 The Reduced Model

Some attempts were made in using the solution of the complete model described above for the solution of the inverse problem, but they have resulted in a high computational cost (several days). For the purpose of speeding-up the inverse problem solution, a reduced model is proposed here. This reduced model involves linear boundary conditions, with a combined heat transfer coefficient that takes into account heat losses by radiation and convection. The mathematical formulation for such a linearized problem in dimensionless form is given by:

$$\frac{1}{\alpha^*} \frac{\partial T^*(r^*, \mu, \tau)}{\partial \tau} = \frac{1}{r^{*2}} \frac{\partial}{\partial r^*} \left(r^{*2} \frac{\partial T^*(r^*, \mu, \tau)}{\partial r^*} \right) + \frac{1}{r^{*2}} \frac{\partial}{\partial \mu} \left((1 - \mu^2) \frac{\partial T^*(r^*, \mu, \tau)}{\partial \mu} \right) \quad \tau > 0, 0 \leq r^* < 1, -1 \leq \mu \leq 1 \quad (8.a)$$

$$k^* \frac{\partial T^*(r^*, \mu; \tau)}{\partial r^*} + Bi_{eff} (T^*(r^*, \mu; \tau) - T_{\infty}^*) = \kappa_{\lambda, laser} q_0^* f(\mu, \mu_0, \tau, \tau_h) \quad r^* = 1, -1 \leq \mu \leq 1, \tau > 0 \quad (8.b)$$

$$T^*(r^*, \mu, \tau) = 1, 0 \leq r^* \leq 1, -1 \leq \mu \leq 1, \tau = 0 \quad (8.c)$$

An analytical solution of the heat conduction problem (8) is obtained through the Classical Integral Transform Technique[41]. In order to reduce the importance of the nonhomogeneous boundary condition (eq. 8.b) on the convergence of the series solution, the solution of the problem is defined as the sum of the solutions of a quasi-steady state heat conduction problem with nonhomogeneous boundary condition (*filtering problem*) and a

transient heat conduction problem with homogeneous boundary conditions (*filtered problem*) by assuming [42,43]:

$$T^*(r^*, \mu, \tau) = T_H^*(r^*, \mu, \tau) + T_F^*(r^*, \mu; \tau) \quad (9)$$

where $T_F^*(r^*, \mu; \tau)$ and $T_H^*(r^*, \mu, \tau)$ are respectively the solutions of the following problems :

$$\frac{1}{r^{*2}} \frac{\partial}{\partial r^*} \left(r^{*2} \frac{\partial T_F^*(r^*, \mu; \tau)}{\partial r^*} \right) + \frac{1}{r^{*2}} \frac{\partial}{\partial \mu} \left((1-\mu^2) \frac{\partial T_F^*(r^*, \mu; \tau)}{\partial \mu} \right) = 0$$

$$\tau > 0, 0 \leq r^* < 1, -1 \leq \mu \leq 1 \quad (10.a)$$

$$k^* \frac{\partial T_F^*(r^*, \mu; \tau)}{\partial r^*} + Bi_{eff} T_F^*(r^*, \mu; \tau) = \kappa_{\lambda, laser} q_0^* f(\mu, \tau_h, \mu_0; \tau) + Bi_{eff} T_\infty^*$$

$$\tau > 0, 0 \leq r^* < 1, -1 \leq \mu \leq 1 \quad (10.b)$$

and

$$\frac{1}{\alpha^*} \frac{\partial T_H^*(r^*, \mu, \tau)}{\partial \tau} = \frac{1}{r^{*2}} \frac{\partial}{\partial r^*} \left(r^{*2} \frac{\partial T_H^*(r^*, \mu, \tau)}{\partial r^*} \right) + \frac{1}{r^{*2}} \frac{\partial}{\partial \mu} \left((1-\mu^2) \frac{\partial T_H^*(r^*, \mu, \tau)}{\partial \mu} \right) - \frac{1}{\alpha^*} \frac{\partial T_F^*(r^*, \mu; \tau)}{\partial \tau}, \quad \tau > 0, 0 \leq r^* < 1, -1 \leq \mu \leq 1 \quad (11.a)$$

$$k^* \frac{\partial T_H^*(r^*, \mu, \tau)}{\partial r^*} + Bi_{eff} T_H^*(r^*, \mu, \tau) = 0, \quad r^* = 1, -1 \leq \mu \leq 1, \tau > 0 \quad (11.b)$$

$$T_H^*(r^*, \mu, \tau) = 1 - T_F^*(r^*, \mu; \tau), \quad 0 \leq r^* \leq 1, -1 \leq \mu \leq 1, \tau = 0 \quad (11.c)$$

The solution of the quasi-steady state problem given by equations (10) is obtained as [41]:

$$T_F^*(r^*, \mu; \tau) = \sum_{n=0}^{\infty} \left(\frac{2n+1}{2} \right) \frac{P_n(\mu) r^{*(n)}}{(k^* n + Bi_{eff})} \left\{ \kappa_{\lambda, laser} q_0^* u(\tau, \tau_h) \bar{g}(n) + Bi_{eff} T_\infty^* \bar{p}(n) \right\} \quad (12)$$

where $n = 0, 1, 2, 3, \dots$ are the eigenvalues associated to the eigenfunctions $P_n(\mu)$, which are Legendre polynomials of order n . The integral transformed terms $\bar{g}(n)$ and $\bar{p}(n)$ appearing in equation (12) are defined respectively as,

$$\bar{g}(n) = \int_{\mu'=-1}^1 g(\mu', \mu_0) P_n(\mu') d\mu' \quad (13.a)$$

$$\bar{p}(n) = \int_{\mu'=-1}^1 P_n(\mu') d\mu' \quad (13.b)$$

The solution of the transient heat conduction problem with homogeneous boundary conditions given by equations (11) is obtained as [41]:

$$T_H^*(r^*, \mu, \tau) = \sum_{n=0}^{\infty} \sum_{p=1}^{\infty} \left(\frac{2n+1}{2N(\lambda_{np})} \right) r^{*-1/2} P_n(\mu) J_{n+1/2}(\lambda_{np}, r^*) \left\{ e^{-\alpha^* \lambda_{np}^2 \tau} \bar{F}(\lambda_{np}, n) - \frac{\kappa_{\lambda, laser} q_0^*}{(k^* n + Bi_{eff})} \frac{J_{n+3/2}(\lambda_{np})}{\lambda_{np}} \bar{g}(n) L(\lambda_{np}) \right\} \quad (14)$$

with the terms $\bar{F}(\lambda_{np}, n)$, $L(\lambda_{np})$, $N(\lambda_{np})$ given respectively by:

$$\bar{F}(\lambda_{np}, n) = \int_0^1 \int_{\mu'=-1}^1 r^{*3/2} P_n(\mu') J_{n+1/2}(\lambda_{np}, r^*) d\mu' dr^* - \frac{J_{n+3/2}(\lambda_{np})}{\lambda_{np} (k^* n + Bi_{eff})} \left\{ \kappa_{\lambda, laser} q_0^* u(\tau, \tau_h) \bar{g}(n) + Bi_{eff} T_{\infty}^* \bar{p}(n) \right\} \quad (15.a)$$

$$L(\lambda_{np}) = \int_{\tau'=0}^{\tau} e^{-\alpha^* \lambda_{np}^2 (\tau - \tau')} \frac{\partial u(\tau', \tau_h)}{\partial \tau'} d\tau' \quad (15.b)$$

$$\frac{1}{N(\lambda_{np})} = \frac{2}{J_{n+1/2}^2(\lambda_{np})} \frac{\lambda_{np}^2}{Bi_{eff} - \frac{k^*}{2} + \lambda_{np}^2 - (n+1/2)^2} \quad (15.c)$$

where $J_{n+1/2}(\lambda_{np}, r^*)$ is the Bessel function of order $n+1/2$, and the terms $\bar{g}(n)$, $\bar{p}(n)$ are given by equations (13).

The eigenvalues λ_{np} are obtained from the following transcendental equation [41]:

$$\lambda_{np} \frac{dJ_{n+1/2}(\lambda_{np})}{d\lambda_{np}} + \frac{Bi_{eff} - k^*}{2} J_{n+1/2}(\lambda_{np}) = 0 \quad (16)$$

It is worth mentioning that, for computational efficiency, the double summation in equation (14) was rearranged in the form of a single summation by reordering the eigenvalues λ_{hp}^2 in increasing order [44]. Furthermore, the different integrals appearing in the analytical solution were precomputed using MATLAB® symbolic computation capabilities.

4. DIRECT PROBLEM AND INVERSE PROBLEM

The *direct problem*, associated with the above physical problem consists in determining the temperature distribution at discrete angular positions on the surface seen by the pyrometer and the corresponding flux collected by the multispectral pyrometer, from the knowledge of initial, boundary conditions, heat source, geometry and thermophysical properties of the solid metal sample.

Regarding the inverse problem, the objective is the estimation of the thermal diffusivity of the solid metal from the measured flux by the multispectral pyrometer. However, the lack of knowledge and/or the uncertainties on the parameters appearing in the mathematical formulation, like the thermal conductivity of the solid metal, its total hemispherical emissivity, the heat losses and the laser parameters (irradiance, spot size, pulse width), must be taken into account. A sensitivity analysis is later performed to determine whether these parameters can be estimated together with the parameter of interest. For the solution of the *inverse problem*, techniques within the Bayesian framework of statistics are used here. These techniques are described next.

5. SOLUTION OF THE INVERSE PROBLEM

Differently from classical inverse problem methodologies, techniques within the Bayesian framework consist of a probabilistic approach with prior and measurement error modelling, which offers a natural support for uncertainties quantification related to the solution of the inverse problem [28,29]. Consider, for the sake of generality, the vector of parameters appearing in the mathematical formulation of the physical problem as:

$$\Psi^T = [\Psi_1, \Psi_2, \dots, \Psi_N] \quad (17)$$

and the vector of the available measurements as

$$\mathbf{Y}^T = [\mathbf{Y}_1, \mathbf{Y}_2, \dots, \mathbf{Y}_I] \quad (18)$$

where N is the number of parameters and \mathbf{Y}_i are vectors of size $S \times 1$, with S the number of measurements sensors, while I is the number of measurements taken with each sensor.

The Bayes theorem is given by:

$$\pi_{posteriori}(\Psi) = \pi(\Psi|Y) = \frac{\pi_{priori}(\Psi)\pi(Y|\Psi)}{\pi(Y)} \quad (19)$$

where, $\pi(Y|\Psi)$ is the likelihood function, which is the statistical model of the measurement errors; and $\pi_{priori}(\Psi)$ is the prior probability density of the parameter vector Ψ , which corresponds to the information available for Ψ before the measurements are taken. The marginal probability density of the measurements $\pi(Y)$ plays the role of a normalizing constant, its calculation is difficult and generally not needed. The posterior probability density $\pi_{posteriori}(\Psi)$ combines the prior probability density of Ψ with the information provided by the measurements Y [28,29,45].

We assume in this work additive measurement errors, so that we can write:

$$Y = \Phi^*(\Psi) + e \quad (20)$$

where Φ^* is the solution of the forward problem, given either by equations (3) or equations (8), and e is a vector that represents the measurement noise. Assuming that e is Gaussian [28], with mean \bar{e} and covariance matrix W_e , the likelihood function is given as:

$$\pi(Y|\Psi) = (2\pi)^{-D/2} |W_e|^{-1/2} \exp \left\{ -\frac{1}{2} [Y - \Phi^*(\Psi) - \bar{e}]^T W_e^{-1} [Y - \Phi^*(\Psi) - \bar{e}] \right\} \quad (21)$$

where, $D=SI$ is the number of measurements.

A common assumption made in the definition of the measurement model given by equations (20) and (21), hereafter referred to as *Conventional Error Model* (CEM), is that $\Phi^*(\Psi)$ actually represents all the physical phenomena involved in the problem, that is, it is computed with an extremely accurate solution of a hypothetical perfect mathematical model. In this work, we assume that such is the case with the numerical solution obtained with the complete model formulation given by equations (3). Therefore, when the complete model is used to compute $\Phi^*(\Psi)$, we assume that the mean of e is zero ($\bar{e} = 0$) and that W_e is the covariance matrix of the measurement errors.

However, obtaining sufficiently accurate solutions in many engineering applications requires the use of complex physical models with sufficiently refined meshes, thus leading to

computational times that are extremely large even with nowadays computer power. Since inverse algorithms usually require several evaluations of the forward problem, the computational cost of the inverse problem solution can be prohibitive, if such complete models are used. A clear solution for these situations is the use of reduced order models. However, the approximation errors between the solutions of the complete and reduced models needed to be accounted for in the likelihood function, as described next.

6. APPROXIMATION ERROR MODEL

In the *Approximation Error Model* (AEM) proposed by Kaipio and Sommersalo [28], the errors related to the use of the reduced model, instead of the complete model, are treated as Gaussian variables that are added to the measurement noise. Statistics of the Approximation Error are computed via Monte Carlo simulations before the solution of the inverse problem, based on the prior distributions for the model parameters that need to have finite variances. In the so called *Enhanced Approximation Error Model* [28,30,31,46–49], the statistics of the approximation error are assumed independent of the model parameters. These offline Monte Carlo simulations can also be used for pre-marginalization of parameters that are not of primary interest for the inverse problem solution [28]. In other words, the approximation error model, besides accounting for modelling errors, may incorporate uncertainties associated with some model parameters that are not really sought in the inverse problem solution.

Consider $\boldsymbol{\Psi}^T = [\mathbf{P}^T, \mathbf{Z}^T]$, where \mathbf{Z} is the vector containing the parameters that are not of primary interest and \mathbf{P} is the vector of sought parameters that are the target of the inverse problem solution. For the problem under study, these are defined respectively as $\mathbf{Z}^T = [Bi_{rad} \ \varepsilon_{\lambda,pyro} \ \kappa_{\lambda,laser} \ q_0^* \ Bi_{conv} \ H_{Mf} \ F_{d1-2}]$ and $\mathbf{P}^T = [\alpha^* \ k^*]$. Equation (20) is then rewritten as:

$$\mathbf{Y} = \boldsymbol{\Phi}^*(\mathbf{P}, \mathbf{Z}) + \mathbf{e} \quad (22)$$

Instead of using the complete model $\boldsymbol{\Phi}^*(\mathbf{P}, \mathbf{Z})$ for the solution of the inverse problem (equations (3) in the present work) and treat \mathbf{P} and \mathbf{Z} as unknown, we set the values of \mathbf{Z} as \mathbf{Z}_0 and make use of the reduced model given by equations (8) to compute $\boldsymbol{\Phi}_{red}^*(\mathbf{P}, \mathbf{Z}_0)$. The analytical solutions given by equations (12) – (16), with a small number of terms in the

eigenfunction expansion, are used to compute $\Phi_{red}^*(\mathbf{P}, \mathbf{Z}_0)$ with low computational times. Thus, equation (22) becomes

$$\mathbf{Y} = \Phi_{red}^*(\mathbf{P}, \mathbf{Z}_0) + \boldsymbol{\eta}(\mathbf{P}, \mathbf{Z}) \quad (23)$$

with

$$\boldsymbol{\eta}(\mathbf{P}, \mathbf{Z}) = \mathbf{v}(\mathbf{P}, \mathbf{Z}) + \mathbf{e} \quad (24)$$

Therefore:

$$\mathbf{v}(\mathbf{P}, \mathbf{Z}) = \Phi^*(\mathbf{P}, \mathbf{Z}) - \Phi_{red}^*(\mathbf{P}, \mathbf{Z}_0) \quad (25)$$

represents the combined errors resulting from model reduction and pre-marginalization of \mathbf{Z} .

It is worth noting that, the modelling error \mathbf{v} is dependent on the sought parameters \mathbf{P} . Since Bayesian inference makes use of probabilistic modelling of the prior information, an estimation of the modelling error can be obtained *a priori* with a Monte Carlo simulation based on the prior distributions for \mathbf{P} and \mathbf{Z} . Then, the solution of the inverse problem can be obtained with the reduced model and the statistics of the modelling and pre-marginalization errors [28–33,47–50]. By assuming that the modelling and the measurements errors are Gaussian with mean $\bar{\boldsymbol{\eta}}_{\mathbf{P},\mathbf{Z}}$ and covariance matrix $\mathbf{W}_{\boldsymbol{\eta}}$, the likelihood function based on $\Phi_{red}^*(\mathbf{P}, \mathbf{Z}_0)$ is given by:

$$\pi(\mathbf{Y}|\mathbf{P}, \mathbf{Z}_0) = (2\pi)^{-D/2} |\mathbf{W}_{\boldsymbol{\eta}}|^{-1/2} \exp\left\{-\frac{1}{2}[\mathbf{Y} - \Phi_{red}^*(\mathbf{P}, \mathbf{Z}_0) - \bar{\boldsymbol{\eta}}_{\mathbf{P},\mathbf{Z}}]^T \mathbf{W}_{\boldsymbol{\eta}}^{-1} [\mathbf{Y} - \Phi_{red}^*(\mathbf{P}, \mathbf{Z}_0) - \bar{\boldsymbol{\eta}}_{\mathbf{P},\mathbf{Z}}]\right\} \quad (26)$$

where:

$$\bar{\boldsymbol{\eta}}_{\mathbf{P},\mathbf{Z}} \approx \bar{\mathbf{v}} + \bar{\mathbf{e}} \quad (27)$$

$$\mathbf{W}_{\boldsymbol{\eta}} \approx \mathbf{W}_{\mathbf{v}} + \mathbf{W}_{\mathbf{e}} \quad (28)$$

In equations (27) and (28), $\bar{\mathbf{v}}$ and $\bar{\mathbf{e}}$ are the means, while $\mathbf{W}_{\mathbf{v}}$ and $\mathbf{W}_{\mathbf{e}}$ are the covariance matrices of \mathbf{v} and \mathbf{e} , respectively. Such as in the *Conventional Error Model* described above, the mean $\bar{\mathbf{e}}$ of the measurement uncertainties can be set to zero after calibration of the

observation sensors. We note that the linear dependence between \mathbf{v} and (\mathbf{P}, \mathbf{Z}) was neglected in equations (27) and (28), which is referred as the *Enhanced Error Model* [28].

With the solutions of the complete and reduced models, given respectively by equations (3) and (12)-(16), the samples $\mathbf{v}_{(m)}$ representing the approximation error can be obtained with Monte Carlo simulations as [28]:

$$\mathbf{v}_{(m)} = \Phi^*(\mathbf{P}_{(m)}, \mathbf{Z}_{(m)}) - \Phi_{red}^*(\mathbf{P}_{(m)}, \mathbf{Z}_0) \quad (29)$$

with $m = 1, 2, \dots, M$. $\mathbf{P}_{(m)}$ and $\mathbf{Z}_{(m)}$ are sampled from the prior probability densities assumed for the parameters \mathbf{P} and \mathbf{Z} , respectively. With the samples $\mathbf{v}_{(m)}$ of the approximation error, the mean $\bar{\mathbf{v}}$ and the covariance matrix \mathbf{W}_v of the approximation error can be computed as:

$$\bar{\mathbf{v}} = \frac{1}{M} \sum_{m=1}^M \mathbf{v}_{(m)} \quad (30)$$

$$\mathbf{W}_v = \frac{1}{M-1} \sum_{m=1}^M (\mathbf{v}_{(m)} - \bar{\mathbf{v}})(\mathbf{v}_{(m)} - \bar{\mathbf{v}})^T \quad (31)$$

By assuming Gaussian prior probability density with mean $\boldsymbol{\mu}^T = [\bar{\alpha}^* \ \bar{k}^*]$ and covariance matrix $\mathbf{V} = \begin{pmatrix} \sigma_{\alpha^*}^2 & 0 \\ 0 & \sigma_{k^*}^2 \end{pmatrix}$ for the vector of unknown parameters \mathbf{P} , and that the likelihood function is given by equation (26), then the posterior probability density of \mathbf{P} is also Gaussian and can be written as:

$$\ln [\pi(\mathbf{P} | \mathbf{Y})] \propto -\frac{1}{2} \left[(D + N) \ln 2\pi + \ln |\mathbf{W}_\eta| + \ln |\mathbf{V}| + S_{MAP}(\mathbf{P}, \mathbf{Z}_0) \right] \quad (32.a)$$

where:

$$S_{MAP}(\mathbf{P}, \mathbf{Z}_0) = [\mathbf{Y} - \Phi_{red}^*(\mathbf{P}, \mathbf{Z}_0) - \bar{\boldsymbol{\eta}}_{\mathbf{P}, \mathbf{Z}}]^T \mathbf{W}_\eta^{-1} [\mathbf{Y} - \Phi_{red}^*(\mathbf{P}, \mathbf{Z}_0) - \bar{\boldsymbol{\eta}}_{\mathbf{P}, \mathbf{Z}}] + [\mathbf{P} - \boldsymbol{\mu}]^T \mathbf{V}^{-1} [\mathbf{P} - \boldsymbol{\mu}] \quad (32.b)$$

A point estimate can be obtained for \mathbf{P} at the maximum of the posterior probability density (MAP). Hence, the estimation procedure becomes an optimization problem, which

consists in the minimization of the maximum a posteriori objective function $S_{MAP}(\mathbf{P}, \mathbf{Z}_0)$ [28,30], that is,

$$\mathbf{P}_{MAP} = \arg \min_{\mathbf{P} \in R^k} S_{MAP}(\mathbf{P}, \mathbf{Z}_0) \quad (33)$$

Such a maximum a posteriori objective function is referred as MAP-AEM in the sequel [28].

For nonlinear estimation problems, such is the case under study, the iterative procedure of the Gauss-Newton method for the minimization of the MAP-AEM objective function is given by:

$$\mathbf{P}^{k+1} = \mathbf{P}^k + [\mathbf{X}^T \mathbf{W}_\eta^{-1} \mathbf{X} + \mathbf{V}^{-1}]^{-1} \{ \mathbf{X}^T \mathbf{W}_\eta^{-1} [\mathbf{Y} - \Phi_{red}^*(\mathbf{P}^k, \mathbf{Z}_0) - \bar{\eta}_{\mathbf{P}, \mathbf{Z}}] + \mathbf{V}^{-1} (\boldsymbol{\mu} - \mathbf{P}^k) \} \quad (34)$$

where the subscript k refers to the iteration number and \mathbf{X} is the sensitivity matrix computed with the estimate \mathbf{P}^k defined by,

$$\mathbf{X} = \left[\frac{\partial \Phi_{red, si}^*}{\partial \mathbf{P}} \right]^T = \begin{bmatrix} \left[\begin{array}{c} \frac{\partial \Phi_{red, 11}^*}{\partial P_1} \\ \vdots \\ \frac{\partial \Phi_{red, S1}^*}{\partial P_1} \\ \vdots \\ \frac{\partial \Phi_{red, 1I}^*}{\partial P_1} \\ \vdots \\ \frac{\partial \Phi_{red, SI}^*}{\partial P_1} \end{array} \right] & \dots & \left[\begin{array}{c} \frac{\partial \Phi_{red, 11}^*}{\partial P_N} \\ \vdots \\ \frac{\partial \Phi_{red, S1}^*}{\partial P_N} \\ \vdots \\ \frac{\partial \Phi_{red, 1I}^*}{\partial P_N} \\ \vdots \\ \frac{\partial \Phi_{red, SI}^*}{\partial P_N} \end{array} \right] \\ \vdots & & \vdots \\ \left[\begin{array}{c} \frac{\partial \Phi_{red, 11}^*}{\partial P_1} \\ \vdots \\ \frac{\partial \Phi_{red, SI}^*}{\partial P_1} \end{array} \right] & \dots & \left[\begin{array}{c} \frac{\partial \Phi_{red, 11}^*}{\partial P_N} \\ \vdots \\ \frac{\partial \Phi_{red, SI}^*}{\partial P_N} \end{array} \right] \end{bmatrix} \quad (35)$$

Approximate posterior covariance estimates for \mathbf{P}_{MAP} can be obtained as follows [28]:

$$\hat{\mathbf{W}}_{\mathbf{P}|\mathbf{Y}} = [\mathbf{X}^T \mathbf{W}_\eta^{-1} \mathbf{X} + \mathbf{V}^{-1}]^{-1} \quad (36)$$

On the other hand, if the chosen estimator is the mean of the posterior probability density, the estimation procedure yields an integration problem and Markov Chain Monte Carlo Methods (MCMC) are used to obtain samples distributed like the posterior. In order to implement the Markov Chain, a probability density $q(\mathbf{P}^{**}, \mathbf{P}^{(t-1)})$ is required, which gives the probability of moving from the current state in the chain $\mathbf{P}^{(t-1)}$ to a new state \mathbf{P}^{**} . The

Metropolis-Hastings algorithm [28,51,52] was used in this work to implement the MCMC method, in addition to the MAP estimator. It can be summarized by the following steps:

1. Sample a Candidate Point \mathbf{P}^{**} from a proposal distribution $q(\mathbf{P}^{**}, \mathbf{P}^{(t-1)})$

2. Calculate:

$$A = \min \left[1, \frac{\pi(\mathbf{P}^{**} | \mathbf{Y})q(\mathbf{P}^{(t-1)}, \mathbf{P}^{**})}{\pi(\mathbf{P}^{(t-1)} | \mathbf{Y})q(\mathbf{P}^{**}, \mathbf{P}^{(t-1)})} \right]$$

3. Generate a random value U which is uniformly distributed on $(0,1)$.

4. If $U \leq A$, define $\mathbf{P}^{(t)} = \mathbf{P}^{**}$. Otherwise, define $\mathbf{P}^{(t)} = \mathbf{P}^{(t-1)}$.

5. Return to step 1 in order to generate the sequence $\{\mathbf{P}^{(1)}, \mathbf{P}^{(2)}, \dots, \mathbf{P}^{(n)}\}$.

Therefore, a sequence that represents the posterior distribution is generated and inference on this distribution is obtained from inference on the samples $\{\mathbf{P}^{(1)}, \mathbf{P}^{(2)}, \dots, \mathbf{P}^{(n)}\}$. We note that the values of $\mathbf{P}^{(i)}$ must be ignored until the chain has converged to equilibrium. For more details on theoretical aspects of the Metropolis-Hastings algorithm and MCMC methods, the reader should consult references [28,51,53,54]

It is worthwhile mentioning that, when the posterior probability density is Gaussian, such as the case herein (see equation (32.a)), the MAP estimate and the posterior mean estimate are the same. We notice also that, while the MAP-estimate obtained with the Gauss-Newton minimization algorithm is generally computationally more appealing than posterior mean estimates obtained with MCMC methods, it provides only a single point estimate in contrast to MCMC methods. Indeed, MCMC methods provide useful information regarding the posterior probability density of the sought parameters from which better decisions can be undertaken.

7. RESULTS AND DISCUSSIONS

In order to generate the simulated measurements for the cases examined below, we consider an AISI stainless steel ball of 3 mm of diameter at uniform initial temperature $T_0 = 1000$ °C. At time $t = 1$ ms, the steel ball is exposed to a square pulse of a Gaussian laser beam of radius $r_0 = 1.3$ mm and duration $t_h = 15$ ms, with power $P = 30$ W. Part of the radiant flux emitted from a spherical cap of 1 mm diameter centred around $\theta = 0^\circ$ on the surface of the steel ball is

observed by the multispectral pyrometer. The absorptivity of the metal sample at the wavelength of the incident laser, its total hemispherical emissivity and its normal spectral emissivities at the different wavelengths of the multispectral pyrometer, are taken as 0.3 [40]. The thermal conductivity and the thermal diffusivity are taken as $k = 23 \text{ Wm}^{-1}\text{K}^{-1}$ and $\alpha = 5.76 \text{ mm}^2\text{s}^{-1}$, respectively [55]. These values are also defined as the reference values. The ambient temperature is taken as $T_\infty = 20 \text{ }^\circ\text{C}$ and assumed to remain constant during the flash experiment. The polar angle θ_{spot} entering in the definition of the reference surface (equation (5.1)) is taken as 19.47° .

7.1 Solution verification

The solution of the complete forward model given by equations (3) is obtained with the finite element software COMSOL Multiphysics®. In order to verify the numerical solution of the problem and to ensure the correct choice of the mesh parameters [56], the numerical solution is compared with the analytical solution of the problem, given by equations (12-16) by assuming a global heat transfer coefficient $h_{eff} = 40 \text{ Wm}^{-1}\text{K}^{-1}$, for both solution methodologies. The analytical solution is implemented with MATLAB®. Figure 3(a) presents a comparison of the temperatures computed with the analytical solution and with COMSOL Multiphysics, for different angular positions θ , at the radial position $r = R$. The relative errors on the computed temperatures are given in figure 3(b), and are smaller than 0.2 %. The fluxes computed at the wavelengths $\lambda = 940 \text{ nm}$ and $\lambda = 1550 \text{ nm}$ of the multispectral pyrometer with the complete model are presented by figure 4.

Tables 1 and 2 illustrate the convergence behaviour of the temperature eigenfunction expansion with the increasing number of terms used in the series solution (equations 12-16), for selected angular positions at $r = R$, at times $t = 6 \text{ ms}$ and $t = 16 \text{ ms}$. As it can be noticed in these tables, convergence is achieved with a small number of terms for time $t = 6 \text{ ms}$, while more than one hundred terms are required to achieve convergence for time $t = 16 \text{ ms}$. Note that, the time $t = 16 \text{ ms}$ corresponds to a discontinuity in the imposed heating, when the laser heating is turn off. Similar behaviour was observed for time $t = 1 \text{ ms}$, which is not presented here for the sake of brevity.

Table 3 compares the computational cost of the numerical and analytical solutions. This table also presents the number of mesh elements used in the discretization of the numerical solution, as well as, the number of eigenfunctions used to compute both quasi-steady state and transient heat conduction problems. The computations were performed in a computer with a processor Intel® i5-6500 CPU, 320 GHz and 16 Gb of RAM. Although the analytical solution

of the reduced model is evaluated only at the radial position $r = R$ for different angular positions, its computational cost is higher as compared to the numerical solution of the complete model obtained with COMSOL Multiphysics®. It is worth mentioning that the commercial code COMSOL Multiphysics® makes an optimal use of the processing unit. We note also that, attempts in using the numerical solution obtained with COMSOL Multiphysics® for the solution of the inverse problem of interest have resulted in a high computational cost. With the aim of reducing this cost for the solution of the inverse problem, the analytical solution given by equations (12-16) is used for the solution of the direct problem, by using a preset fixed low truncation order in the eigenfunction expansion. That is, instead of the prescribed convergence criterion on the relative error (10^{-5}) used for the results given in tables 1 and 2, the number of terms used in the temperature eigenfunction is set arbitrarily. It is worthwhile noting in table 3 that, the relative high computational cost of the analytical solution is essentially due to the computation of the solution of the transient heat conduction problem with homogeneous boundary conditions. Thus, the number of terms used in the eigenfunction expansion of the latter was set to 10, leading to a computation cost of 11 s for the reduced model with low truncation order.

7.2 Sensitivity analysis and D-Optimal Design

Before the solution of the inverse parameter estimation problem is investigated, an analysis of the sensitivity coefficients must be performed. It is desirable to have linearly independent sensitivity coefficients with large magnitudes, for an accurate estimation of the parameters [57,58]. We make use of reduced sensitivity coefficients in the analysis presented below. The reduced sensitivity coefficients are defined as the original sensitivity coefficients multiplied by their corresponding parameters, so that the measured flux can serve as a basis of comparison to identify small magnitudes and linearly dependent parameters [57,58]. In this work, the reduced dimensionless sensitivity coefficients J_{ij} with respect to parameters Ψ_j of the complete forward model are defined as:

$$J_{ij} = \Psi_j \frac{\partial \Phi_{si}^*}{\partial \Psi_j} \quad (37)$$

and were computed with forward finite differences.

The sensitivity analysis is performed with the complete forward model and the effects of the laser beam size incident on the steel ball, the temporal profile of the pulse and the position of the surface seen by the pyrometer (surface S1 centred on $\theta_1 = 0^\circ$, surface S2 centred on $\theta_2 = 20^\circ$, surface S3 centred on $\theta_3 = 60^\circ$), as illustrated in figure 5, were investigated. In order

to perform the sensitivity analysis, the maximum temperature increase of the heated surface was set to 50 °C to have a reasonable approximation of the assumption of constant physical properties with respect to the temperature variation. The sensitivity coefficients computed for the different wavelengths of the multispectral pyrometer presented the same behaviour, with the largest flux magnitudes obtained for the wavelength $\lambda = 1550$ nm. Therefore, the analysis below is presented only for this wavelength. Moreover, for the case under study, flux measurements obtained at the wavelength $\lambda = 1550$ nm and $\lambda = 940$ nm are the only useful information, since the lower measured threshold power of the multispectral pyrometer is 50 nW.

The influence of the incident laser beam size on the sensitivity coefficients was examined for beam diameters of 1 mm and 2.6 mm, for square pulses with $P = 13$ W and $t_h = 3$ ms, as well as for $P = 30$ W and $t_h = 15$ ms. These values were chosen so that the maximum temperature increase of the heated surface was limited to 50 °C. Figures 6 present the transient behaviour of the sensitivity coefficients of the different model parameters, computed by considering measurements taken over the surface S_1 . The dimensionless flux is also presented in figures 6. It can be noticed in these figures that, the sensitivity coefficients of thermal diffusivity and thermal conductivity obtained for the incident laser beam size of 2.6 mm are of larger magnitudes than those corresponding to the laser beam size of 1 mm. This is due to the fact that more energy is provided to the steel ball in the case of an incident laser beam size of 2.6 mm for the same maximum temperature increase of 50 °C. The beam size of 2.6 mm is therefore favourable for the estimation of the parameters of interest, because the sensitivity coefficients present large magnitudes. It can be observed in figures 6 that the sensitivity coefficients of the parameters of interest (thermal diffusivity and thermal conductivity) are an order of magnitude smaller than the dimensionless flux and than the sensitivity coefficients of the emissivity $\epsilon_{\lambda,pyro}$, the form factor F_{d1-2} and the flux losses H_{Mi} . The analysis of the sensitivity coefficients suggests the possibility of simultaneously estimating the thermal diffusivity and the thermal conductivity of the steel ball. However, the remaining model parameters have to be known, since they are correlated and the magnitudes of their sensitivity coefficients are one order larger or of the same order of those for the parameters of interest.

For the analysis of the effect of the position of the surface where the measurements are taken by the pyrometer on the sensitivity coefficients, a square pulse of power $P = 30$ W, with pulse duration $t_h = 15$ ms is considered, with the laser beam diameter of 2.6 mm. Figures 6(b),

7 (a),(b) present the transient behaviour of the sensitivity coefficients computed at surfaces S_1 , S_2 and S_3 , respectively. It can be noticed in these figures that the magnitudes of the sensitivity coefficients calculated at surface S_1 are the largest. The sensitivity coefficients computed at surface S_2 present a similar behaviour, but with magnitudes smaller than those at S_1 , in particular those of the thermal diffusivity and of the thermal conductivity. Although the sensitivity coefficients of the thermal diffusivity and of the thermal conductivity computed at surface S_3 seem less correlated, they are two orders of magnitude smaller than the flux observed by the pyrometer. The measurements of the flux obtained at surface S_1 are therefore more appropriate for the estimation of the parameters of interest, because the sensitivity coefficients of the parameters of interest present large magnitudes.

Regarding the effect of the temporal profile of the incident laser pulse on the sensitivity coefficients, a square pulse and an exponentially decaying pulse were examined (see equations 7.a and 7.b). Figures 8 present the sensitivity coefficients for the case of an exponentially decaying pulse ($P=30$ W, $t_h = 15$ ms), while the case of a square pulse is given in figure 6(b). It can be noticed in these figures that the case of a square pulse presents sensitivity coefficients of the same magnitude with those of the exponentially decaying pulse. Moreover, one can note in figure 8 that the thermal diffusivity and the thermal conductivity are strongly correlated in the case of the exponentially decaying pulse. It is also clear from these figures that the thermal diffusivity and the thermal conductivity tend to be uncorrelated after the heating is ceased.

From the foregoing analysis of the sensitivity coefficients, it can be concluded that the measurements taken at the surface S_1 , with a square pulse and an incident beam size of 2.6 mm, result in better conditions for the simultaneous estimation of the thermal diffusivity and thermal conductivity of the levitated metal sample. However, the remaining model parameters should be known, due to their relative high sensitivity coefficients.

Together with the sensitivity analysis, the maximization of the determinant of the Fisher information matrix ($|\mathbf{J}^T \mathbf{J}|$) plays an important role in inverse parameter estimation [57,58]. Optimum experiments can be designed by maximizing the determinant of the information matrix, in addition to the analysis of the sensitivity coefficients performed above.

For a case involving two sensors, each element of the information matrix $\mathbf{F}_{m,n}$, $m,n=1,\dots,N$, of the matrix $\mathbf{F}=\mathbf{J}^T \mathbf{J}$ is given by [57,58]:

$$\mathbf{F}_{m,n} = [\mathbf{J}^T \mathbf{J}]_{m,n} = \sum_{s=1}^2 \sum_{i=1}^I \left(\frac{\partial \Phi_{si}^*}{\partial P_m} \right) \left(\frac{\partial \Phi_{si}^*}{\partial P_n} \right) \quad m, n = 1, \dots, N \quad (38)$$

where I is the number of measurements taken with each sensor and N is the number of unknown parameters. Such an analysis is performed for the parameters of interest, namely the thermal diffusivity and the thermal conductivity of the levitating metal sample.

The maximization of the determinant of the Fisher information matrix is performed by assuming available flux measurements from the multispectral pyrometer at the wavelengths $\lambda = 1550$ nm and $\lambda = 940$ nm, at a rate of 0.5 kHz on surface S_1 . In order to evaluate the effect of the heating rate, different laser powers with different pulse durations were considered, again with the maximum temperature rise at the heated of 50 °C. Figure 9 presents the variation of the determinant of the Fisher information matrix with respect to time for different heating rates. Note in this figure that the heating rate has no significant effects on the determinant of the Fisher information matrix, although $P = 30$ W and $t_h = 15$ ms yields the maximum of information. We note that, the minimum output power of the available laser is $P = 30$ W.

In order to investigate the effect of the pulse duration on the determinant of the Fisher information matrix, the maximum temperature rise of the heated surface is now allowed to reach 100 °C. This temperature increase amounts to 10 % of the initial temperature, as suggested by Bayazitoglu and co-workers [1]. The analysis is performed for a fixed laser output power $P = 30$ W, with beam width of 2.6 mm. Figure 10 presents the effect of the variation of the pulse duration on the determinant of the Fisher information matrix. It can be noticed in this figure that the increase of the pulse duration increases the determinant of the Fisher information matrix and such a positive effect is less significant for $t > 45$ ms. It can also be noticed that the variation of the determinant is quite small for $t > 150$ ms,. Thus, the final time of the experiment can be taken as 150 ms and the pulse duration as 60 ms, which results in a maximum temperature increase of 90 °C in the sample.

7.3 Parameter estimation

The robustness of the proposed methodology for the simultaneous estimation of the thermal diffusivity and thermal conductivity with respect to the noise level on the experimental data, as well as with the quality of the prior information on the model's parameters, is now investigated with synthetic data. The synthetic data are generated by adding zero mean Gaussian random noise \mathbf{e} with standard deviation σ to the solution of the complete forward problem as follows:

$$\mathbf{Y} = \Phi^*(\bar{\mathbf{P}}, \bar{\mathbf{Z}}) + \mathbf{e} \quad (39)$$

where $\bar{\mathbf{P}}, \bar{\mathbf{Z}}$ represent the vectors of “true” parameters. The objective of the inverse problem is to obtain an estimate for $\mathbf{P}^T = [\alpha \ k]$ from the synthetic data \mathbf{Y} , by using the reduced forward model $\Phi_{red}^*(\mathbf{P}, \mathbf{Z}_0)$, while accounting for the uncertainties on the auxiliary parameters $\mathbf{Z}^T = [Bi_{rad} \ \varepsilon_{\lambda,pyro} \ \kappa_{\lambda,laser} \ q_0^* \ Bi_{conv} \ H_{Mi} \ F_{d1-2}]$. We recall that \mathbf{Z}_0 is a vector containing point values of \mathbf{Z} . It is also worth recalling that the sensitivity analysis has revealed that these parameters are correlated, thus, they cannot be estimated simultaneously with the parameters of primary interest. Moreover, the magnitudes of the sensitivity coefficients of these auxiliary parameters are of the same order of magnitude or larger than those of the parameters of interest $\mathbf{P}^T = [\alpha \ k]$. As a consequence, estimates of these parameters with associated uncertainties have to be obtained from other sources, independent of the experiment of the front-face flash method under study. These estimates could be obtained from literature or through dedicated experiments. For instance, the irradiance q_0^* can be calculated from both measurements of the laser output power and of the beam size, respectively, with a power meter and a beam analyser. Likewise, the parameters H_{Mi} are obtained from the calibration of the multispectral pyrometer and were reported in [38]. The heat losses by radiation and convection, characterized respectively by Bi_{rad} and Bi_{conv} could be determined from a cooling experiment of the levitating sample of metal in the same experimental conditions, prior to the flash experiment itself. This would be similar to the two-step procedure for thermal diffusivity estimation of levitating sample of metal suggested in [1,2], where the heat losses, essentially by radiation, were obtained by calibrating a lumped capacity model for a cooling experiment. It is worth noting that, for the case under study, the heat losses by radiation and convection are correlated. Hence, they need to be estimated in separate experiments. Two approaches are envisioned in order to determine the heat losses for the proposed experiment. The first consists in using radiative flux measurements taken at different wavelengths of the multispectral pyrometer, in order to estimate simultaneously the transient temperature and the emissivity [52]. Given, the estimates of the emissivity and of the transient temperature, the heat losses by convection can be obtained from the heat balance equation, assuming valid the lumped capacity formulation, either through a simple algebraic calculation [59,60] or via a parameter estimation technique. The second approach relies on the Bayesian calibration of a conjugated heat transfer model for the estimation of the total hemispherical emissivity, given uncertainties on the remaining thermophysical properties and on the surface temperature

measurements taken during the cooling. The convective heat losses can thus be computed from the conjugate heat transfer model with the estimated emissivity. Such a detailed physical model of the cool-down experiment of the levitated sample of metal was developed in COMSOL Multiphysics and solves a non-isothermal flow problem with temperature-dependent properties. As a consequence, one evaluation of the direct problem presents a high computational cost, thus, the Bayesian inversion algorithm proposed in [61] is being investigated for computational efficiency. Irrespective of the approach adopted to obtain the heat losses, the heat capacity and the density of the material being characterized are required. On the other hand, some data on heat capacities of metallic materials at high temperatures can be found in the literature[8,9,11,55].

Figure 11 presents a comparison of the flux obtained from the solution of the complete forward model and the reduced forward model at the wavelength $\lambda = 1\ 550$ nm of the multispectral pyrometer. One can note some discrepancies between the fluxes. It is worth recalling that, the analytical solution defined as the reduced model is computed with a few number of terms in the eigenfunction expansion and that the heat losses by radiation and convection are defined with a global heat transfer coefficient. The complete forward model given by equations (3) is solved with COMSOL Multiphysics® and the solution is considered sufficiently accurate. The synthetic data included in figure 11 are obtained according to equation (39), by adding Gaussian random noise of zero mean and standard-deviation $\sigma = 1\ \% \max(\Phi^*)$ to the solution of the complete forward model obtained with COMSOL Multiphysics®. In order to avoid an inverse crime [28], a more refined finite element mesh is used for the generation of the synthetic data than that used for the computation of the approximation error statistics.

For the calculation of the statistics of the approximation error, the Gaussian prior probability densities given by table 4 were considered. We note in this table that the means of the prior probability densities of all the parameters are purposely set to values larger than those used to generate the synthetic data, except for the irradiance and the absorptivity. The computed statistics of the modelling errors account not only for the model reduction error, but also for the uncertainties/misspecification on the auxiliary parameters contained in \mathbf{Z}_0 . Monte Carlo simulations are then performed from the prior probability densities given in table 4 and the statistics of the approximation error are computed according to equations (30) and (31), by using both complete forward and reduced models. The number of samples used in the calculation of the statistics of the approximation error is set to 10 000.

For the solution of the inverse problem of simultaneous estimation of the thermal diffusivity and thermal conductivity of the steel sphere, the prior probability densities associated to the thermal diffusivity and thermal conductivity given in table 4 were used. Both Newton-Gauss algorithm for the minimization of MAP objective function and the Metropolis-Hastings algorithm were used, jointly with the Approximation Error Model, for the solution of the inverse problem.

Given the synthetic measurements obtained with the complete model, the reduced model and the statistics of the approximation error, which include the model reduction errors and errors related to the inaccurately known auxiliary parameters, the thermal diffusivity and the thermal conductivity obtained with both estimation algorithms are given below. Table 5 presents the results obtained with the Newton-Gauss minimization of the MAP-AEM objective function, including the initial guess for the parameters. One can note that accurate estimates of the sought parameters were obtained. The latter are close to their exact values, and present relatively small standard deviations. These results demonstrate the effectiveness of the proposed methodology for the simultaneous estimation of the thermal diffusivity and thermal conductivity through the minimization of the MAP-AEM objective function.

Figure 12 presents the states of the Markov chains for the thermal conductivity and the thermal diffusivity. One can note a rapid convergence of the states of the Markov chain to an equilibrium distribution around the exact values of the sought parameters. Figure 13 compares the prior distributions of the parameters and the posterior distributions obtained from the MCMC samples. The histograms of the marginal posteriors for the thermal diffusivity and thermal conductivity are also shown in this figure. The first 1 000 states of the Markov chain were discarded (burn-in period) for the computation of the statistics. One can note in these figures that the information provided by the measurements has resulted in a considerable reduction of the initial uncertainties on the thermal diffusivity and thermal conductivity. Moreover, the most likely values of these parameters are concentrated around their exact values. Table 6 presents the posterior mean estimates of the thermal diffusivity and thermal conductivity, as well as, the associated standard deviations, which are relatively small.

It can be noticed in tables 5 and 6 that the estimated thermal conductivities and thermal diffusivities are very close to their exact values, and present relatively small standard deviations. Furthermore, the results obtained by combining the AEM and the Newton-Gauss or MCMC-MH algorithms demonstrate the robustness of the proposed methodology, given that the auxiliary parameters, except the irradiance and the absorptivity, where *pre-marginalized* around inaccurate values (overestimated at 5 % of their exact values) and with

large uncertainties (10 %). Regarding, the computational cost, while the MAP estimate is obtained in five minutes, the Markov chains were generated in about eight hours. However, as mentioned earlier, one might be interested in obtaining detailed statistical information on the estimates, which are readily made available from MCMC sampling methods, but not with MAP.

8. CONCLUSIONS

In this work, techniques within the Bayesian framework, namely the Gauss-Newton minimization of the *maximum a posteriori objective function* and the Markov chain Monte Carlo method, coded in the form of the Metropolis-Hastings algorithm, were used for the thermal characterization of aerodynamically levitated solid sample of metals at high temperatures. The proposed methodology is based on the front-face flash method with laser excitation and contactless transient flux measurements available from a multispectral pyrometer. An analysis of the sensitivity coefficients with respect to the model parameters reveals that the thermal diffusivity and the thermal conductivity of the levitated metal sample can be estimated, provided that other auxiliary parameters are known. These auxiliary parameters are correlated and with magnitude of their sensitivity coefficients comparable to those of the sought parameters. In order to deal with the possible sources of inaccuracies and uncertainties of the auxiliary parameters, the approximation error model is jointly used with the estimation algorithms. Moreover, modelling errors between the actual heat conduction model with nonlinear boundary conditions and the heat conduction with linear boundary conditions are accounted for, as well as, the low truncation order of the analytical solution developed for the heat conduction model with linear boundary conditions. Simulated transient flux measurements were used in the inverse analysis. The proposed methodology enables to get accurate and simultaneous estimates of the thermal diffusivity and thermal conductivity of the sample of metal, given the specified prior information. This work has provided the theoretical background and also highlighted the measurements necessary to estimate the thermal properties of interest. Future works will be directed on the experimental validation of the proposed methodology.

ACKNOWLEDGEMENTS

The authors are thankful for the support provided by CNRS, French National Research Center for the fostering of science.

AUTHOR DISCLOSURE STATEMENT

There are no relationships of all authors with any people or organizations that could inappropriately influence (bias) this work.

REFERENCES

- [1] Y. Bayazitoglu, P.V.R. Suryanarayana, U.B. Sathuvalli, High-temperature thermal diffusivity determination procedure for solids and liquids, *J. Thermophys. Heat Transf.* 4 (1990) 462–468. doi:10.2514/3.209.
- [2] F. Shen, J.M. Khodadadi, M.C. Woods, J.K.R. Weber, B.Q. Li, Containerless Thermal Diffusivity Determination of High-Temperature Levitated Spherical Specimen by Extended Flash Methods: Theory and Experimental Validation, *J. Heat Transfer.* 119 (1997) 210–219. doi:10.1115/1.2824211.
- [3] I. Egry, Physical Property Measurements of Liquid Metals at High Temperatures under Microgravity, *Mater. Trans.* 45 (2004) 3235–3240. doi:10.2320/matertrans.45.3235.
- [4] R.W. Hyers, G. Trapaga, B. Abedian, Laminar-turbulent transition in an electromagnetically levitated droplet, *Metall. Mater. Trans. B Process Metall. Mater. Process. Sci.* 34 (2003) 29–36. doi:10.1007/s11663-003-0052-7.
- [5] R.W. Hyers, Fluid flow effects in levitated droplets, *Meas. Sci. Technol.* 16 (2005) 394–401. doi:10.1088/0957-0233/16/2/010.
- [6] K.C. Mills, Thermophysical property requirements for modelling of high temperature processes, in: *Microgravity Res. Appl. Phys. Sci. Biotechnol. First Int. Symp.* 10-15 Septemeber, 2000 Sorrento, Italy, European Space Agency, ESA SP-454, 2001., p. 555, 2001. <http://adsabs.harvard.edu/full/2001ESASP.454..555M>.
- [7] P.C. Nordine, J.K.R. Weber, J.G. Abadie, Properties of high-temperature melts using levitation, *Pure Appl. Chem.* 72 (2000) 2127–2136. doi:10.1351/pac200072112127.
- [8] R.K. Wunderlich, H.J. Fecht, Modulated electromagnetic induction calorimetry of reactive metallic liquids, *Meas. Sci. Technol.* (2005). doi:10.1088/0957-0233/16/2/011.
- [9] H. Kobatake, H. Fukuyama, I. Minato, T. Tsukada, S. Awaji, Noncontact modulated laser calorimetry of liquid silicon in a static magnetic field, *J. Appl. Phys.* 104 (2008). doi:10.1063/1.2966455.
- [10] T. Tsukada, H. Fukuyama, H. Kobatake, Determination of thermal conductivity and emissivity of electromagnetically levitated high-temperature droplet based on the periodic laser-heating method: Theory, *Int. J. Heat Mass Transf.* 50 (2007) 3054–3061. doi:10.1016/j.ijheatmasstransfer.2006.12.026.
- [11] H. Fukuyama, H. Kobatake, K. Takahashi, I. Minato, T. Tsukada, S. Awaji, Development of modulated laser calorimetry using a solid platinum sphere as a reference, *Meas. Sci. Technol.* 18 (2007) 2059–2066. doi:10.1088/0957-0233/18/7/036.

- [12] T. Tsukada, K. ichi Sugioka, T. Tsutsumino, H. Fukuyama, H. Kobatake, Effect of static magnetic field on a thermal conductivity measurement of a molten droplet using an electromagnetic levitation technique, *Int. J. Heat Mass Transf.* 52 (2009) 5152–5157. doi:10.1016/j.ijheatmasstransfer.2009.04.020.
- [13] I. Egry, D. Holland-Moritz, Levitation methods for structural and dynamical studies of liquids at high temperatures, *Eur. Phys. J. Spec. Top.* 196 (2011) 131–150. doi:10.1140/epjst/e2011-01424-1.
- [14] P.C. Nordine, D. Merkley, J. Sickel, S. Finkelman, R. Telle, A. Kaiser, R. Prieler, A levitation instrument for containerless study of molten materials, *Rev. Sci. Instrum.* 83 (2012). doi:10.1063/1.4770125.
- [15] P.F. Paradis, T. Ishikawa, G.W. Lee, D. Holland-Moritz, J. Brillo, W.K. Rhim, J.T. Okada, Materials properties measurements and particle beam interactions studies using electrostatic levitation, *Mater. Sci. Eng. R Reports.* (2014). doi:10.1016/j.mser.2013.12.001.
- [16] B.Q. Li, Effect of convection on the measurement of thermophysical properties using levitated droplets, *Ann. N. Y. Acad. Sci.* 1077 (2006) 1–32. doi:10.1196/annals.1362.059.
- [17] W.J. Parker, R.J. Jenkins, C.P. Butler, G.L. Abbott, Flash method of determining thermal diffusivity, heat capacity, and thermal conductivity, *J. Appl. Phys.* (1961). doi:10.1063/1.1728417.
- [18] ASTM International, E1461. Standard test method for thermal diffusivity by the flash method., 2013. doi:10.1520/E1461-13.
- [19] B. Remy, A. Degiovanni, Parameters estimation and measurement of thermophysical properties of liquids, *Int. J. Heat Mass Transf.* (2005). doi:10.1016/j.ijheatmasstransfer.2005.03.004.
- [20] D. Maillet, C. Moyne, B. Rémy, Effect of a thin layer on the measurement of the thermal diffusivity of a material by a flash method, *Int. J. Heat Mass Transf.* (2000). doi:10.1016/S0017-9310(00)00020-X.
- [21] T. Lechner, E. Hahne, Finite pulse time effects in flash diffusivity measurements, *Thermochim. Acta.* (1993). doi:10.1016/0040-6031(93)80434-C.
- [22] A. Degiovanni, M. Laurent, Une nouvelle technique d'identification de la diffusivité thermique pour la méthode « flash », *Rev. Phys. Appliquée.* (1986). doi:10.1051/rphysap:01986002103022900.
- [23] R.D. Cowan, Pulse method of measuring thermal diffusivity at high temperatures, *J.*

- Appl. Phys. (1963). doi:10.1063/1.1729564.
- [24] R.D. Cowan, Proposed Method of Measuring Thermal Diffusivity at High Temperatures, *J. Appl. Phys.* (1961). doi:10.1063/1.1736235.
- [25] L.M. Clark, R.E. Taylor, Radiation loss in the flash method for thermal diffusivity, *J. Appl. Phys.* (1975). doi:10.1063/1.321635.
- [26] J.A. Cape, G.W. Lehman, Temperature and finite pulse-time effects in the flash method for measuring thermal diffusivity, *J. Appl. Phys.* (1963). doi:10.1063/1.1729711.
- [27] F. Shen, J.M. Khodadadi, Combined thermocapillary and buoyancy-driven convection within short-duration pulse-heated liquid droplets, *Numer. Heat Transf. Part A Appl.* 36 (1999) 839–857. doi:10.1080/104077899274480.
- [28] J. Kaipio, E. Somersalo, *Statistical and Computational Inverse Problems*, Springer-Verlag, 2004.
- [29] J.P. Kaipio, C. Fox, The Bayesian framework for inverse problems in heat transfer, *Heat Transf. Eng.* 32 (2011) 718–753. doi:10.1080/01457632.2011.525137.
- [30] V. Kolehmainen, T. Tarvainen, S.R. Arridge, J.P. Kaipio, Marginalization of Uninteresting Distributed Parameters in Inverse Problems - Application To Diffuse Optical Tomography, *Int. J. Uncertain. Quantif.* 1 (2011) 1–17. doi:10.1615/Int.J.UncertaintyQuantification.v1.i1.10.
- [31] A. Pulkkinen, V. Kolehmainen, J.P. Kaipio, B.T. Cox, S.R. Arridge, T. Tarvainen, Approximate marginalization of unknown scattering in quantitative photoacoustic tomography, *Inverse Probl. Imaging.* (2014). doi:10.3934/ipi.2014.8.811.
- [32] M. Mozumder, T. Tarvainen, J.P. Kaipio, S.R. Arridge, V. Kolehmainen, Compensation of modeling errors due to unknown domain boundary in diffuse optical tomography., *J. Opt. Soc. Am. A. Opt. Image Sci. Vis.* 31 (2014) 1847–55. doi:10.1364/JOSAA.31.001847.
- [33] B. Lamien, H.R.B. Orlande, G.E. Elicabe, Particle Filter and Approximation Error Model for State Estimation in Hyperthermia, *J. Heat Transfer.* 139 (2017). doi:10.1115/1.4034064.
- [34] T. Hibiya, I. Egry, Thermophysical property measurements of high temperature melts: Results from the development and utilization of space, *Meas. Sci. Technol.* 16 (2005) 317–326. doi:10.1088/0957-0233/16/2/001.
- [35] D. Langstaff, M. Gunn, G.N. Greaves, A. Marsing, F. Kargl, Aerodynamic levitator furnace for measuring thermophysical properties of refractory liquids, *Rev. Sci. Instrum.* 84 (2013). doi:10.1063/1.4832115.

- [36] G. Pottlacher, K. Aziz, A. Schmon, Containerless experimental techniques to obtain thermophysical properties of liquid metals and alloys at high temperatures and density data for liquid aluminium, in: 8th Int. Conf. Electromagn. Process. Mater., Cannes, France, 2015. <hal-01335586> .
- [37] L. Dejaeghere, T. Pierre, M. Carin, P. Le, Design and development of an induction furnace to characterize molten metals at high temperatures, *High Temp. - High Press.* 47 (2018) 23–49.
- [38] B. Lamien, D.L.E. Maux, M. Courtois, M. Carin, P.L.E. Masson, H. Orlande, Développement d ’ un dispositif expérimental pour la caractérisation de métaux autour du point de fusion par lévitation aérodynamique, in: Société Française Therm. SFT 2018, Pau, France, 2018.
- [39] C. Balaji, *Essentials of Radiation Heat Transfer*, Ane Books Pvt. Ltd., 2014.
- [40] J.R. Howell, P.M. Menguc, R. Siegel, *Thermal Radiation Heat Transfer*, 6th ed., CRC Press, 2002.
- [41] M.N. Ozisik, *Heat Conduction*, John Wiley & Sons, Inc., New York, NY, 1993.
- [42] J.N.. Cotta, Renato M., Knupp, D.C, Quaresma, *Analytical Methods in Heat Transfer*, in: F.A. Kulacki, V.K. Dhir, M.P. Mengüç (Eds.), *Handb. Therm. Sci. Eng.*, Springer Open Ltd, 2017. doi:10.1007/978-3-319-32003-8.
- [43] R.M. Cotta, M.D. Mikhailov, *Heat Conduction: Lumped Analysis, Integral Transforms, Symbolic Computation*, John Wiley & Sons, Chichester, 1997.
- [44] E.J. Corrêa, R.M. Cotta, H.R.B. Orlande, On the reduction of computational costs in eigenfunction expansions of multidimensional diffusion problems, *Int. J. Numer. Methods Heat Fluid Flow.* (1997). doi:10.1108/09615539710185569.
- [45] H.R.B. Orlande, *Inverse Problems in Heat Transfer: New Trends on Solution Methodologies and Applications*, *J. Heat Transfer.* (2012). doi:10.1115/1.4005131.
- [46] S.R. Arridge, J.P. Kaipio, V. Kolehmainen, M. Schweiger, E. Somersalo, T. Tarvainen, M. Vauhkonen, Approximation errors and model reduction with an application in optical diffusion tomography, *Inverse Probl.* 22 (2006) 175–195. doi:10.1088/0266-5611/22/1/010.
- [47] A. Nissinen, L.M. Heikkinen, V. Kolehmainen, J.P. Kaipio, Compensation of errors due to discretization, domain truncation and unknown contact impedances in electrical impedance tomography, *Meas. Sci. Technol.* 20 (2009) 105504. doi:10.1088/0957-0233/20/10/105504.
- [48] A. Nissinen, L.M. Heikkinen, J.P. Kaipio, The Bayesian approximation error approach

- for electrical impedance tomography—experimental results, *Meas. Sci. Technol.* 19 (2008) 015501. doi:10.1088/0957-0233/19/1/015501.
- [49] A. Nissinen, V.P. Kolehmainen, J.P. Kaipio, Compensation of modelling errors due to unknown domain boundary in electrical impedance tomography, *IEEE Trans. Med. Imaging.* 30 (2011) 231–242. doi:10.1109/TMI.2010.2073716.
- [50] S.R. Arridge, J.P. Kaipio, V. Kolehmainen, M. Schweiger, E. Somersalo, T. Tarvainen, M. Vauhkonen, Approximation errors and model reduction with an application in optical diffusion tomography, *Inverse Probl.* 22 (2006) 175–195. doi:10.1088/0266-5611/22/1/010.
- [51] H.S. Migon, D. Gamerman, *Statistical Inference : an Integrated Approach*, London, 1999.
- [52] H.R.B. Orlande, O. Fudym, D. Maillet, R.M. Cotta, *Thermal Measurements and Inverse Techniques*, CRC Press, Boca Raton, FL, 2011.
- [53] P.M. Lee, *Bayesian Statistics: An Introduction*, 2012. doi:10.2307/1270551.
- [54] X.-L.M. Steve Brooks, Andrew Gelman, Galin L. Jones, *Handbook of Markov Chain Monte Carlo*, CRC Press, Boca Raton, FL, 2011.
- [55] K.C. Mills, *Recommended Values of Thermophysical Properties for Selected Commercial Alloys*, Woodhead Publishing, 2002. doi:10.1016/B978-1-84569-990-1.50021-1.
- [56] ASME V&V 20, *Standard for Verification and Validation in Computational Fluid Dynamics and Heat Transfer*, Am. Soc. Mech. Eng. (2009). doi:10.1016/S0160-4120(97)89943-6.
- [57] M.N. Ozisik, H.R.B. Orlande, *Inverse heat transfer*, Taylor & Francis, New York, NY, 2000.
- [58] K.A. Woodbury, *Inverse engineering handbook*, 2003.
- [59] F. Greffrath, R. Prieler, R. Telle, A new method for the estimation of high temperature radiant heat emittance by means of aero-acoustic levitation, *Infrared Phys. Technol.* (2014). doi:10.1016/j.infrared.2014.08.013.
- [60] G. Lohöfer, S. Schneider, Heat balance in levitation melting: Sample cooling by forced gas convection in Argon, *High Temp. - High Press.* 45 (2016) 255–271.
- [61] T. Cui, C. Fox, M.J. O’Sullivan, Bayesian calibration of a large-scale geothermal reservoir model by a new adaptive delayed acceptance Metropolis Hastings algorithm, *Water Resour. Res.* (2011). doi:10.1029/2010WR010352.

TABLE CAPTIONS

Table 1. Illustration of convergence behaviour of temperature field eigenfunction expansion ($t = 6$ ms)

Table 2: Illustration of convergence behaviour of temperature field eigenfunction expansion ($t = 16$ ms)

Table 3: Mesh/Number of eigenfunctions and computation cost of the numerical and analytical solutions.

Table 4: Prior Probability Densities used in the computation of the Approximation Error

Table 5: Results obtained with the Gauss-Newton minimization of the MAP-AEM objective function

Table 6: Results obtained with the MCMC-MH-AEM

FIGURE CAPTIONS

Figure 1: Experimental facility

Figure 2: Physical Model

Figure 3: Dimensional Transient Temperatures at Selected Angular Positions for $r = R$ (a); with Associated Relative Errors (b)

Figure 4: Calculated flux at $\bar{\lambda}_5 = 940$ nm (a), $\bar{\lambda}_6 = 1\,550$ nm (b)

Figure 5: Surfaces observed by the pyrometer

Figure 6: Effect of the incident laser beam size on the sensitivity coefficients (top) 1 mm; (bottom) 2.6 mm

Figure 7: Effect of the position of the surface seen by the pyrometer on the sensitivity coefficients, (top) surface S_2 ; (bottom) surface S_3

Figure 8: Effect of the temporal profile of the pulse on the sensitivity coefficients for an exponentially decaying pulse.

Figure 9: Effect of the heating rate on the determinant of the Fisher information matrix

Figure 10: Effect of the pulse duration on the determinant of the Fisher information matrix

Figure 11: Comparison of the dimensionless fluxes computed with the complete and reduced forward models at the wavelength $\lambda = 1\,550$ nm of the multispectral pyrometer

Figure 12: States of the Markov Chain for the thermal diffusivity and for the thermal conductivity

Figure 13: Scatter Distribution of the Samples representing: The Prior Distribution with Associated Marginal (a); the Posterior Distribution with Associated Marginal (b)

Table 1: Illustration of convergence behaviour of temperature field eigenfunction expansion ($t = 6$ ms), with associated relative error (%)

θ ($^{\circ}$)	$N=30$	$N=48$	$N=66$	$N=84$	$N=102$	$N=120$
0	1031.052(0.17)	1029.420(0.01)	1029.326(0.00)	1029.321(0.00)	1029.321(0.00)	1029.321
3.5	1029.606(0.15)	1028.114(0.01)	1028.036(0.00)	1028.032(0.00)	1028.032(0.00)	1028.032
7	1027.941(0.14)	1026.590(0.01)	1026.525(0.00)	1026.521(0.00)	1026.521(0.00)	1026.521
11	1026.320(0.13)	1025.096(0.01)	1025.039(0.00)	1025.035(0.00)	1025.035(0.00)	1025.035
19	1023.378(0.10)	1022.366(0.01)	1022.317(0.00)	1022.314(0.00)	1022.314(0.00)	1022.314

Table 2: Illustration of convergence behaviour of temperature field eigenfunction expansion ($t = 16$ ms) , with associated relative error (%)

θ (°)	$N=30$	$N=48$	$N=66$	$N=84$	$N=102$	$N=120$
0	1042.087(0.55)	1045.334(0.24)	1046.652(0.12)	1047.191(0.06)	1047.629(0.02)	1047.871
3.5	1040.433(0.51)	1043.515(0.22)	1044.644(0.11)	1045.135(0.06)	1045.550(0.02)	1045.774
7	1038.591(0.47)	1041.478(0.20)	1042.467(0.10)	1042.917(0.06)	1043.310(0.02)	1043.517
11	1036.797(0.44)	1039.486(0.18)	1040.385(0.09)	1040.801(0.05)	1041.176(0.02)	1041.369
19	1033.466(0.38)	1035.775(0.16)	1036.574(0.08)	1036.939(0.05)	1037.281(0.02)	1037.453

Table 3: Mesh/Number of eigenfunctions and computation cost of the numerical and analytical solutions.

Solutions	Number of mesh elements/ eigenfunctions	Computational time (s)
Complete model	1595 elements	50
Quasi steady-state problem	18 terms	1
Transient Problem with Homogeneous boundary conditions	102 terms	76
Reduced Model with low truncation order	28 terms	11

Table 4: Prior Probability Densities used in the computation of the Approximation Error

Property / Parameter	Dimensionless Parameter	Prior Distribution	Mean	Standard deviation
Thermal diffusivity	α^*	Gaussian	$\bar{\alpha}^* = 1.09 \alpha^*$	$0.15 \bar{\alpha}^*$
Thermal conductivity	k^*	Gaussian	$\bar{k}^* = 1.09 k^*$	$0.15 \bar{k}^*$
Irradiance	q_0^*	Gaussian	$\bar{q}_0^* = q_0^*$	$0.05 \bar{q}_0^*$
Radiative Biot number	Bi_{rad}	Gaussian	$\bar{Bi}_{rad} = 1.05 Bi_{rad}$	$0.05 \bar{Bi}_{rad}$
Absorptivity at $\lambda_{laser} = 1\ 060\ \text{nm}$	$\mathcal{K}_{\lambda,laser}$	Gaussian	$\bar{\mathcal{K}}_{\lambda,laser} = \mathcal{K}_{\lambda,laser}$	$0.05 \bar{\mathcal{K}}_{\lambda,laser}$
Normal spectral emissivity at λ_{filter}	$\mathcal{E}_{\lambda,pyro}$	Gaussian	$\bar{\mathcal{E}}_{\lambda,pyro} = 1.05 \mathcal{E}_{\lambda,pyro}$	$0.05 \bar{\mathcal{E}}_{\lambda,pyro}$
Amplitude correction	H_{Mi}	Gaussian	$\bar{H}_{Mi} = 1.05 H_{Mi}$	$0.1 \bar{H}_{Mi}$
Form factor	F_{d1-2}	Gaussian	$\bar{F}_{d1-2} = 1.05 F_{d1-2}$	$0.1 \bar{F}_{d1-2}$
Convective Biot number	Bi_{conv}	Gaussian	$\bar{Bi}_{conv} = 1.05 Bi_{conv}$	$0.1 \bar{Bi}_{conv}$

Table 5: Results obtained with the Gauss-Newton minimization of the MAP-AEM objective function

	MAP-AEM –Reduced model with overestimated and uncertain auxiliary parameters			
Parameter	Exact	Initial guess	Estimate	Standard deviation
$k(\text{Wm}^{-1}\text{K}^{-1})$	23	18.4	23.55	1.04
$\alpha(\text{mm}^2\text{s}^{-1})$	5.76	4.61	5.81	0.21

Table 6: Results obtained with the MCMC-MH-AEM

	MCMC-MH – Reduced model + AEM and overestimated auxiliary parameters			
Parameter	Exact	Initial state	Estimate	Standard deviation
$k(\text{Wm}^{-1}\text{K}^{-1})$	23	18.4	23.56	0.96
$\alpha(\text{mm}^2\text{s}^{-1})$	5.76	4.61	5.71	0.19

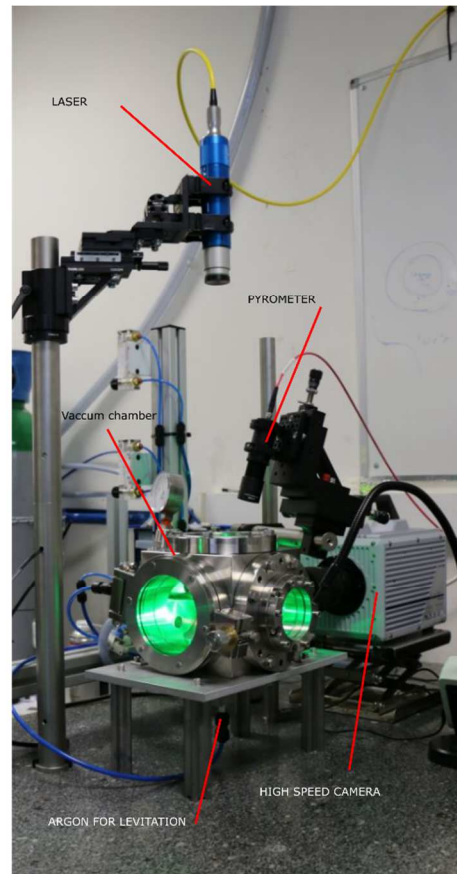
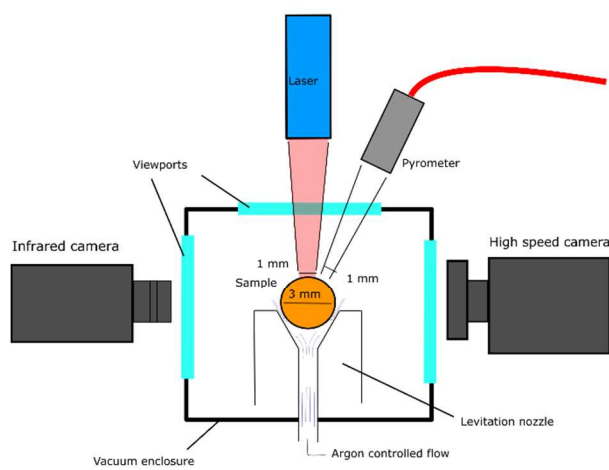


Figure 1: Experimental facility

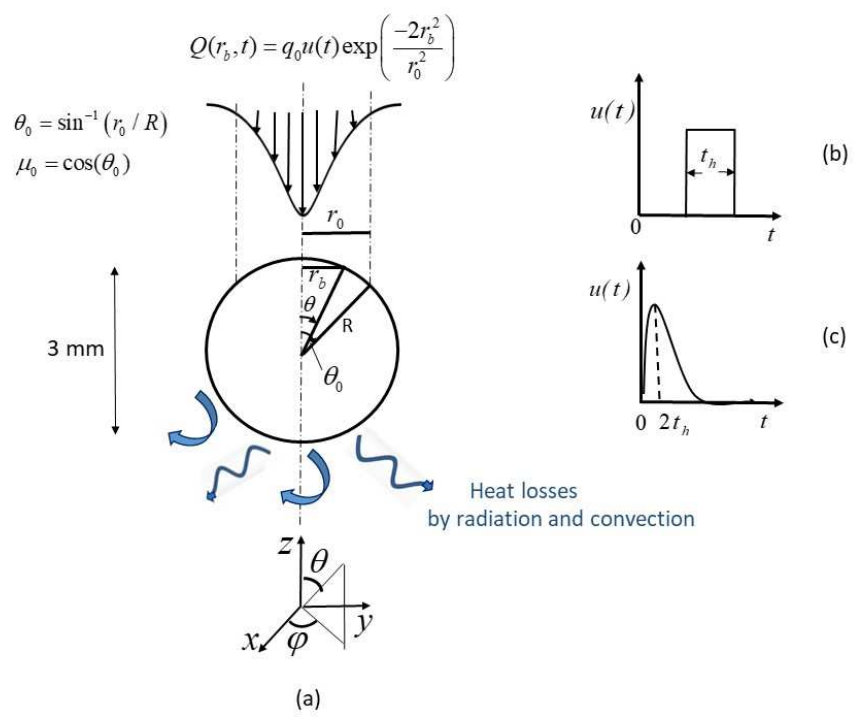


Figure 2: Physical Model

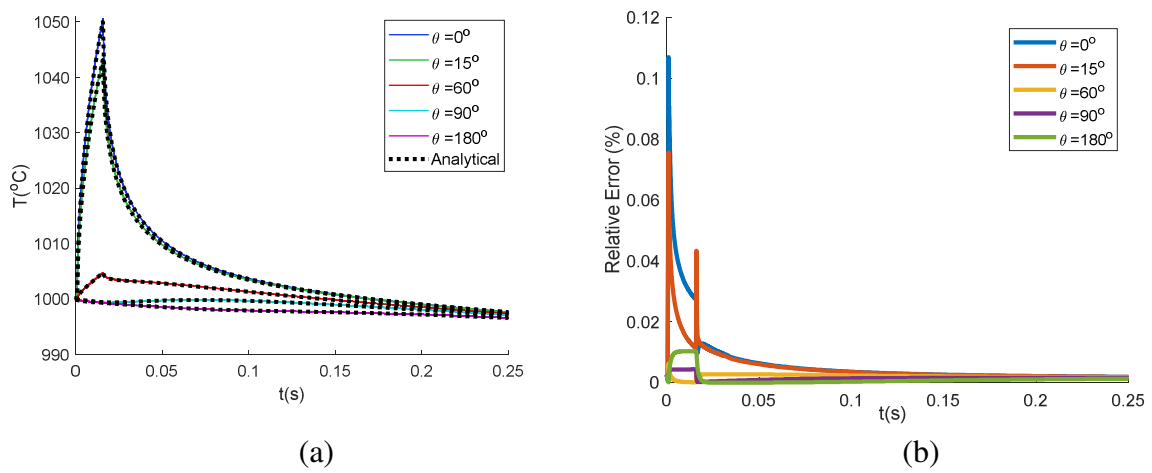
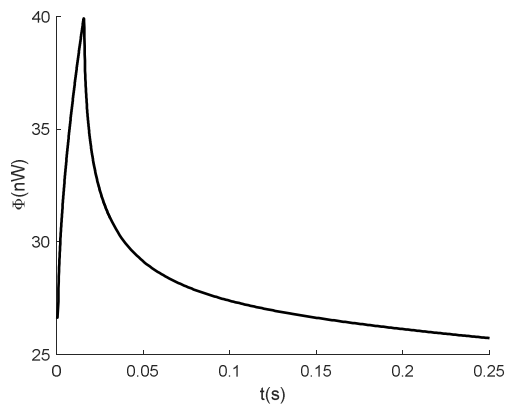
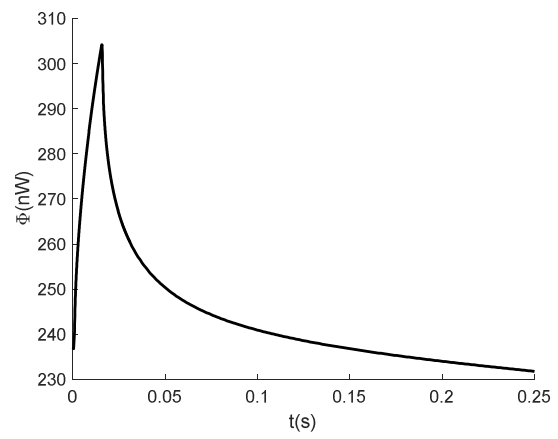


Figure 3: Dimensional Transient Temperatures at Selected Angular Positions for $r = R$ (a); with Associated Relative Errors (b)



(a)



(b)

Figure 4: Calculated radiative flux at $\lambda_5 = 940$ nm (a), $\lambda_6 = 1550$ nm (b)

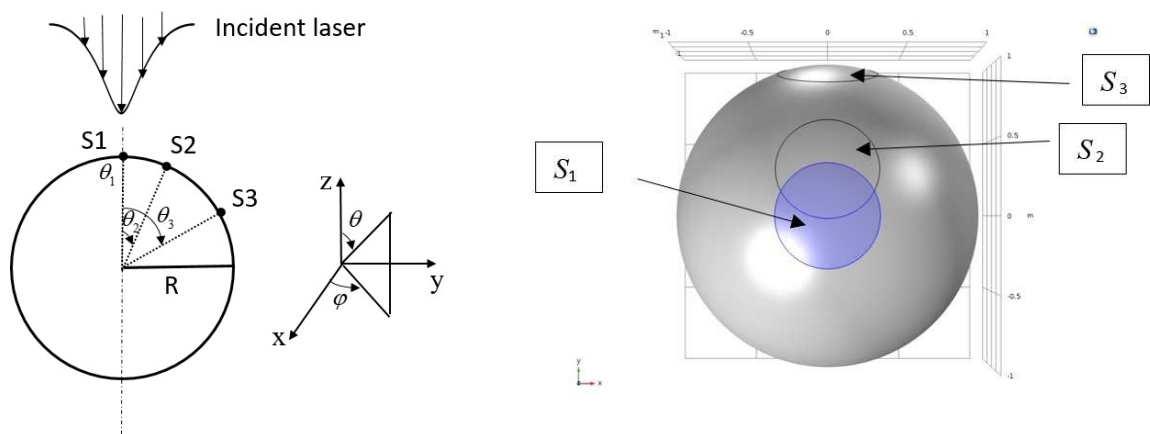
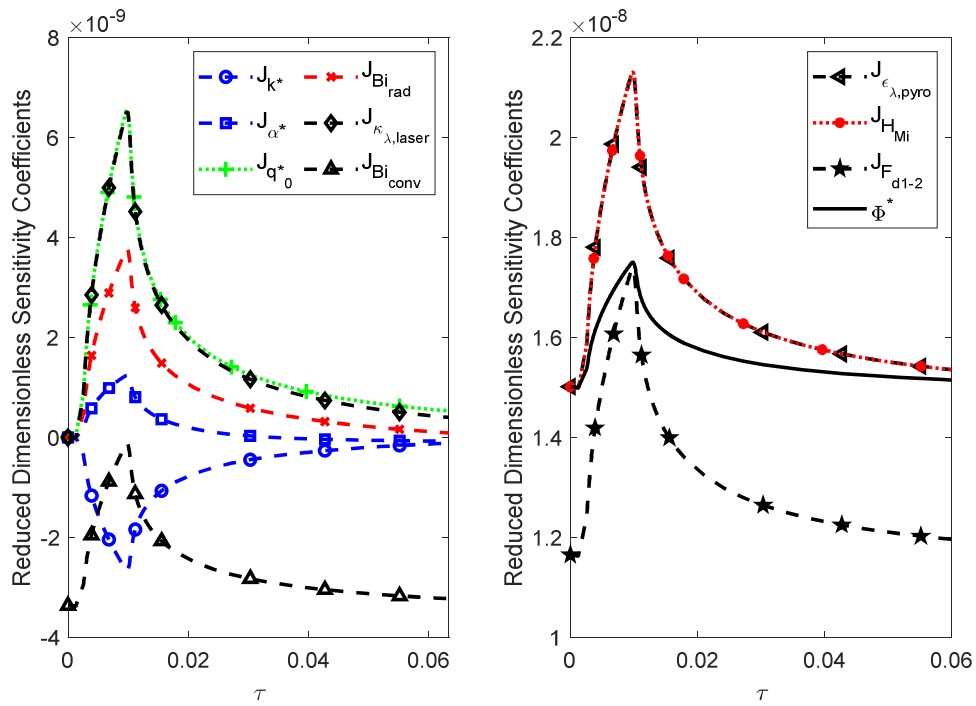
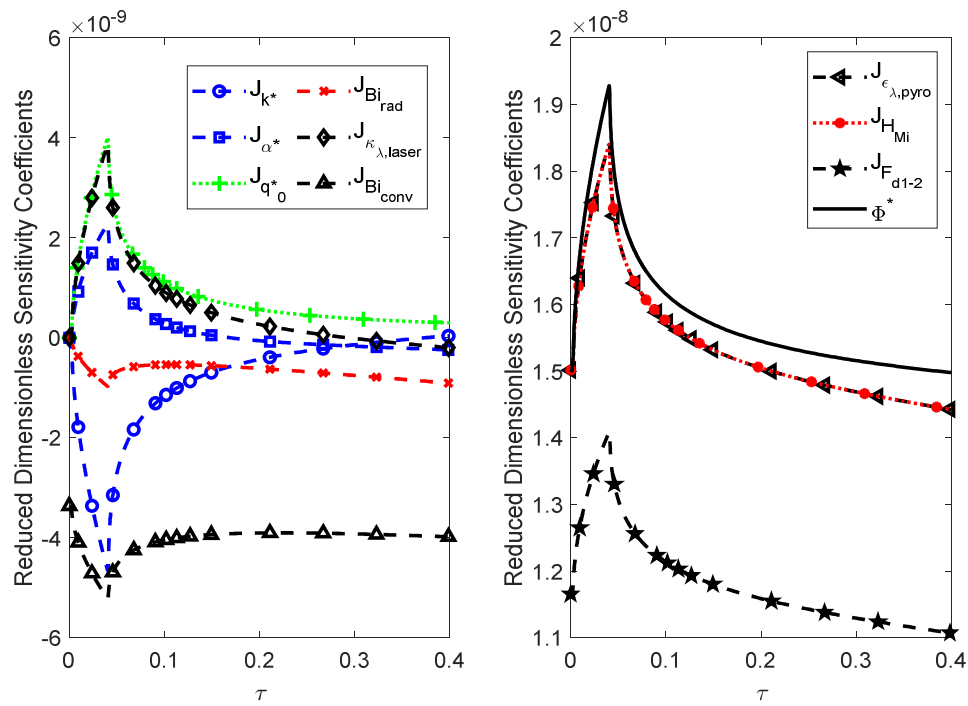


Figure 5: Surfaces observed by the pyrometer

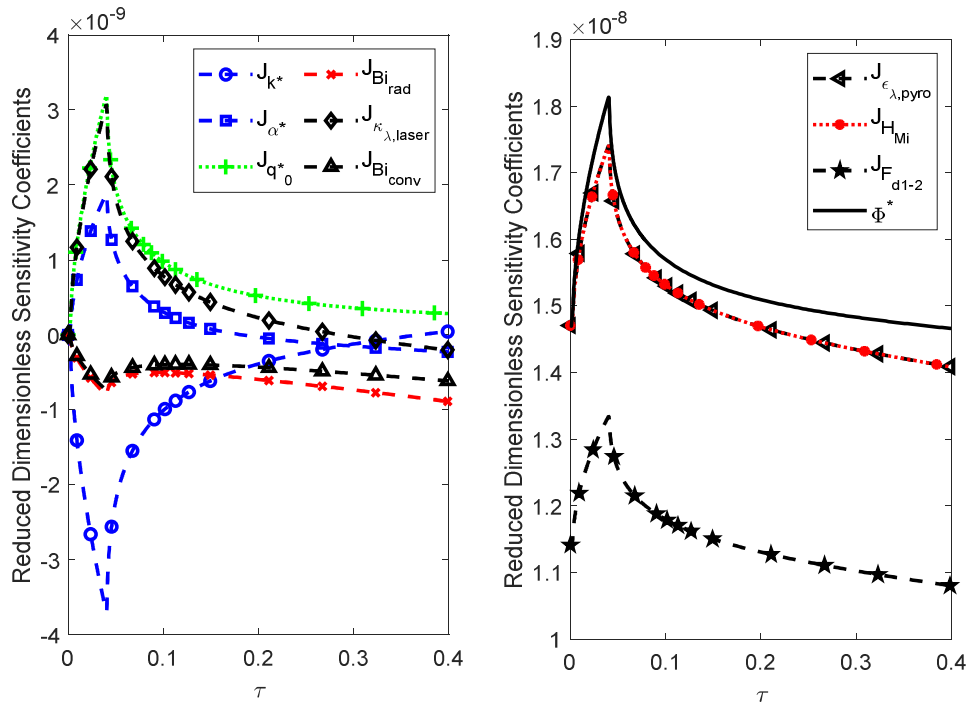


(a)

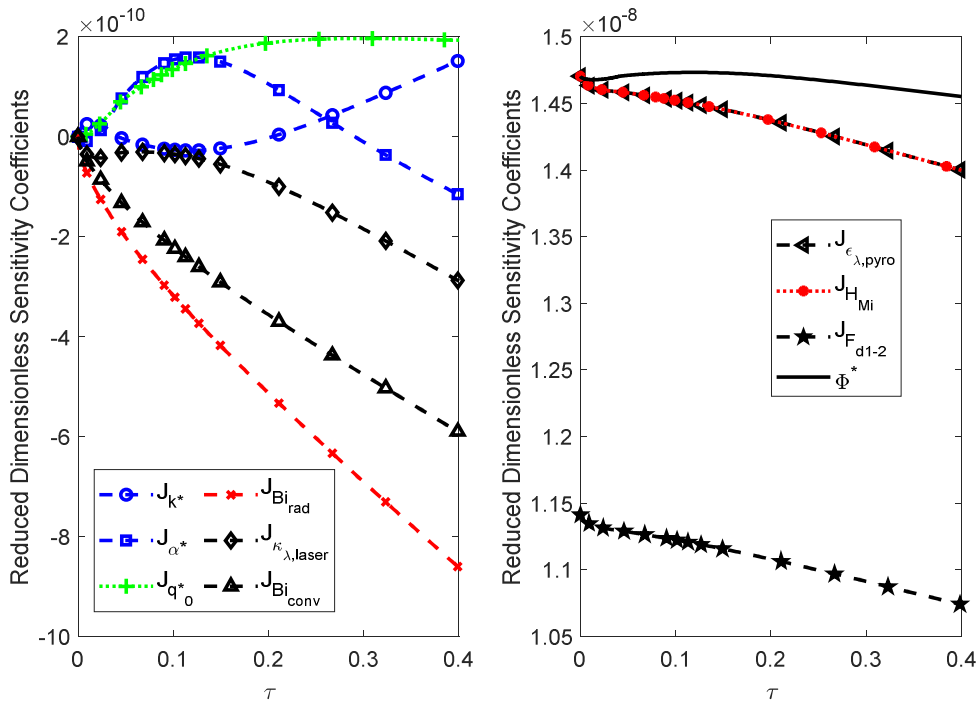


(b)

Figure 6: Effect of the incident laser beam size on the sensitivity coefficients (a) 1 mm; (b) 2.6 mm



(a)



(b)

Figure 7: Effect of the position of the surface seen by the pyrometer on the sensitivity coefficients, (a) surface S_2 ; (b) surface S_3

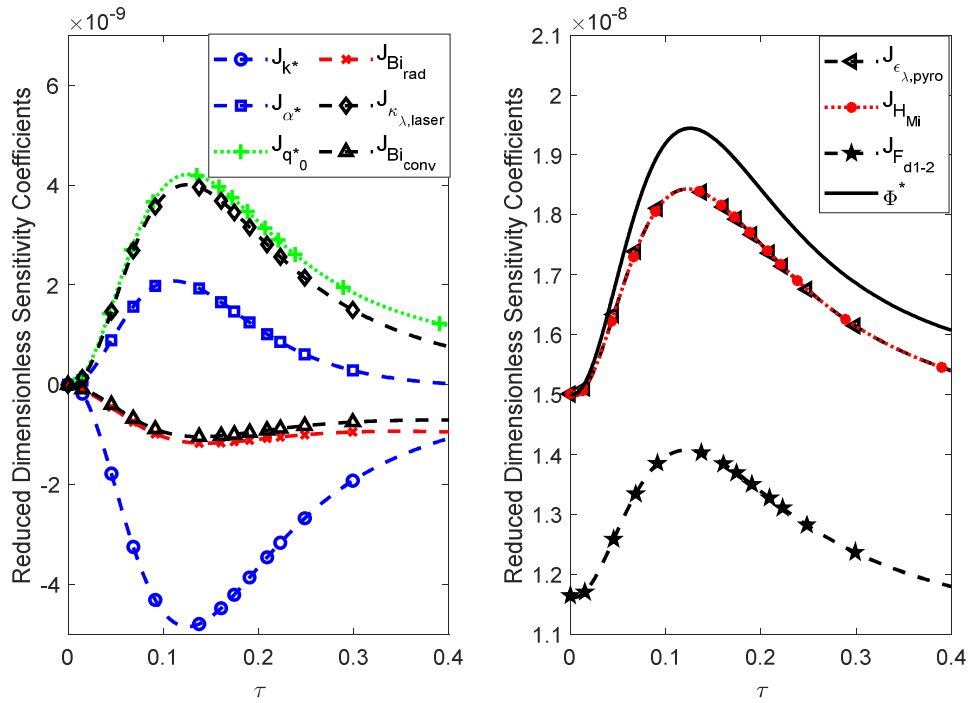


Figure 8: Effect of the temporal profile of the pulse on the sensitivity coefficients for an exponentially decaying pulse

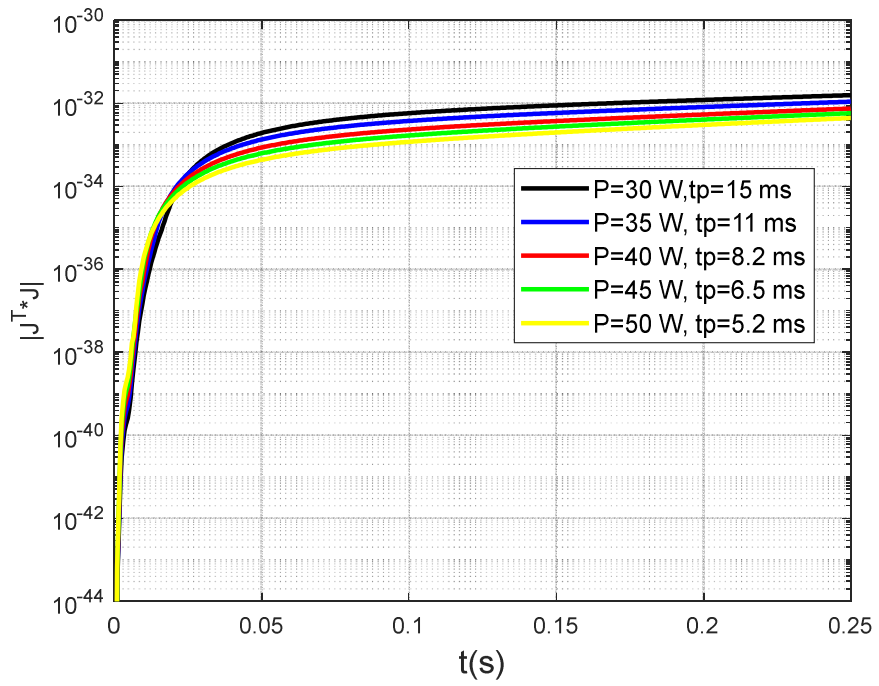


Figure 9: Effect of the heating rate on the determinant of the Fisher information matrix

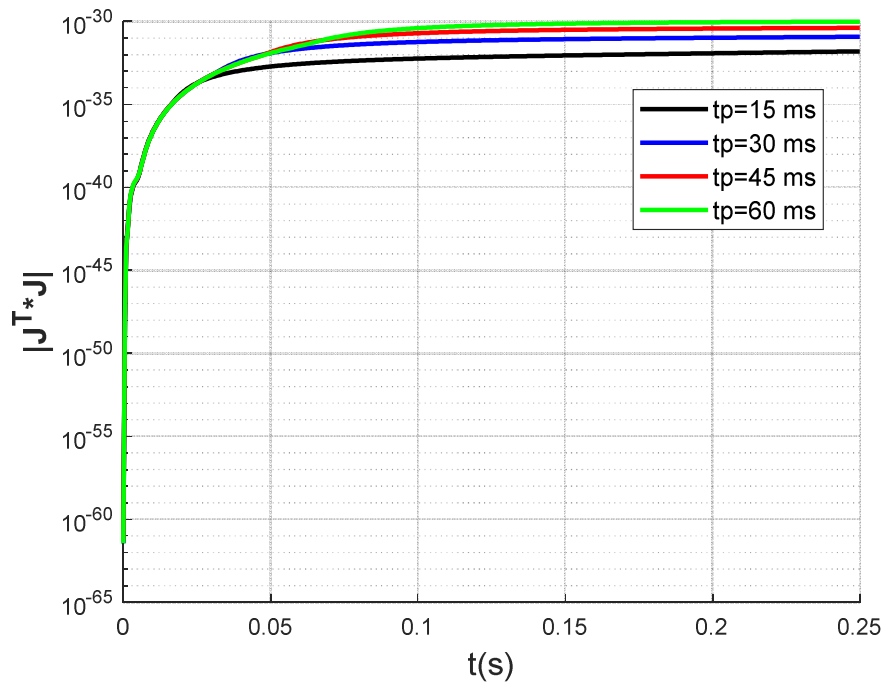


Figure 10: Effect of the pulse duration on the determinant of the Fisher information matrix

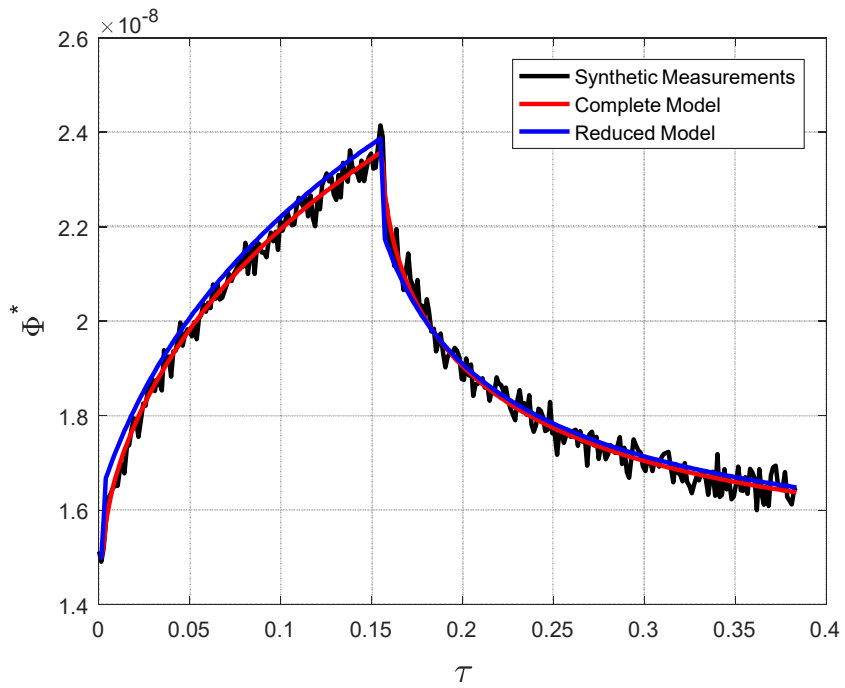


Figure 11: Comparison of the dimensionless fluxes computed with the complete and reduced forward models at the wavelength $\lambda = 1\,550$ nm of the multispectral pyrometer

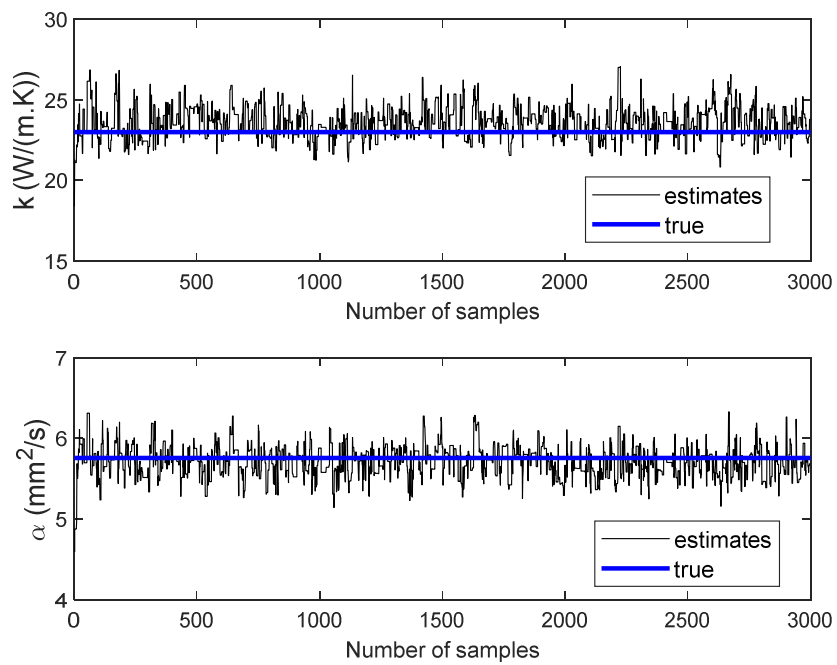


Figure 12: States of the Markov Chain for the thermal diffusivity and for the thermal conductivity

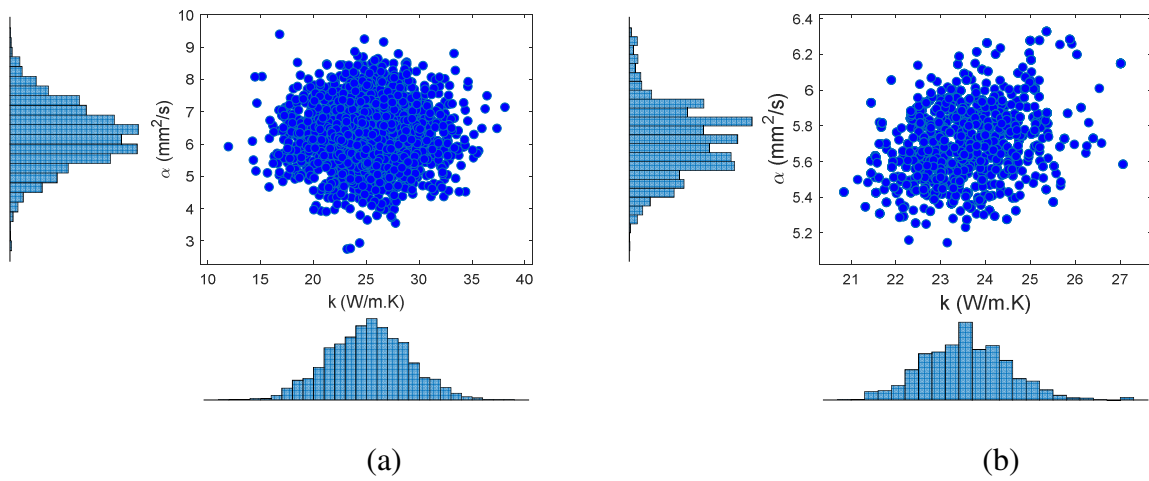


Figure 13: Scatter Distribution of the Samples representing: The Prior Distribution with Associated Marginal (a); the Posterior Distribution with Associated Marginal (b)